ION CYCLOTRON HEATING OF THE JET PLASMA

M. Brambilla

IPP 4/217 April 1984

MAX-PLANCK-INSTITUT FÜR PLASMAPHYSIK

8046 GARCHING BEI MÜNCHEN

MAX-PLANCK-INSTITUT FÜR PLASMAPHYSIK

GARCHING BEI MÜNCHEN

ION CYCLOTRON HEATING OF THE JET PLASMA

M. Brambilla

IPP 4/217 April 1984

Die nachstehende Arbeit wurde im Rahmen des Vertrages zwischen dem Max-Planck-Institut für Plasmaphysik und der Europäischen Atomgemeinschaft über die Zusammenarbeit auf dem Gebiete der Plasmaphysik durchgeführt.

Marco Brambilla

IPP 4/217

Ion Cycloton Heating of the JET Plasma

April 1984

Abstract

The numerical code RAYIC has been used to investigate three ion cyclotron heating scenarios of the JET plasma: a) He_3^{++} minority in a Hydrogen plasma; b) first harmonic heating of a Deuterium plasma; c) H^+ minority in a Hydrogen plasma.

The dependence of absorption on the discharge parameters (density, temperature, minority concentration, etc.) is discussed in terms of elementary damping mechanisms: wave conversion, Ion Cyclotron damping, electron transit time and Landau Damping.

All three methods are found to be satisfactorily efficient for typical JET extended phase performances. Use of quadruple antennae can further considerably enhance the single transit absorption.

This report has been prepared under the contract JB1/9020 between the IPP-Euratom Association and JET

1 - INTRODUCTION

In this report we present some systematic investigation of Ion cyclotron heating of JET, performed using the numerical code RAYIC /1/. This code models coupling, propagation and absorption of electromagnetic waves in large axisymmetric plasmas in the ion cyclotron frequency domain.

The core of RAYIC is a ray-tracing subroutine which follows the propagation of the compressional Alfven wave in arbitrary axisymmetric plasma configurations. The dispersion relation is written in the warm-plasma approximation, neglecting the electron inertia. The initial conditions for the ray and power transport equations are provided by a 3-D plane layered model of the antenna. The output of the antenna package consists of the spectral distribution of the radiated power among partial waves of different toroidal wavenumber n_φ, and, for each n_φ, of the distribution of the power flux across a wavefront in the poloidal direction. The power transport equation takes into account cyclotron damping at the fundamental and first harmonic cyclotron resonance for the ions, and transit time and Landau damping for the electrons. Finally, a semi-analytic treatment of mode conversion in the geometry of a tokamak allows to establish the fate of the power reaching a wave resonance (ion-ion resonances or confluence with the first Ion Bernstein wave near $\omega = 2\Omega_c$), where ray tracing breaks down. Details about the physical model underlying the code are given in /2/ and /3/.

Planned ICH of JET will use generators tunable between 25 and 55 Mhz, to allow maximum flexibility in the choice of the heating mechanism /4/. In the present work we have considered three heating scenarios compatible

with the available frequency range:

1) $^3He^{++}$ minority in a Hydrogen plasma (Section 2);

2) first harmonic resonance of a deuterium plasma (Section 3);

3) H^+ minority in a Deuterium plasma (Section 4).

The meridian cross section of the MHD equilibrium used throughout this study is shown in Fig. 1. In this context, we note that the ability of RAYIC to deal with non-circular plasmas was particularly useful to obtain quantitatively reliable results in the case of JET: for example, focusing of the waves near the plasma center is much less pronounced in JET than in a circular plasma.

The discharge parameters have been chosen to be typical of those expected in the extended performance phase of JET operation /4/. They are listed in Table I for a standard ohmically heated target plasma. In the examples, quantities whose value is not explicitly mentioned are identical to those of this standard case.

The density and temperature profiles assumed are shown in Fig. 2. When central values have been changed, the shape of the profiles has not been modified. The surface averaged current density has been taken proportional to $T_e^{3/2}$, normalized to the total current I. The resulting profile of the safety factor is also shown in Fig. 2. Note that because of the noncircular cross-section, all profiles have been plotted against a flux variable ψ ($0 \leq \psi \leq 1$) labeling magnetic surfaces. The relation between and position can be desumed by inspection of Fig. 1.

In most examples, the waves are assumed to be launched by four dipole antennas, located on the equatorial plane on the low magnetic field side

(LMFS), and equally spaced in the toroidal direction around the device. Their parameters are listed in Table II. In a few cases, the effect of using quadrupole antennas instead of the conventional dipole ones has been investigated. In all runs, the initial wavefront for ray-tracing has been chosen at $\psi = 0.8$, about 15 cm inside the plasma in front of the antennas. For the profiles of Fig. 2, the conditions for the validity of the Eikonal approximation are already well satisfied there.

Due to the large dimensions of the JET plasma and the high absorption efficiency found in most cases, the assumptions of both the antenna model and of ray tracing are well justified. This of course does not imply that RAYIC can answer every question about ICH of large tokamak plasmas. It is therefore important to understand the meaning and limitations of the results presented below.

Many of these results are presented in term of the absorption efficiency for each species of particles in the plasma, defined as

$$\eta_{ABS} = \frac{P_{ABS}}{P_{COUPL}} \tag{1}$$

where P_{COUPL} is the total coupled power, and P_{ABS} is the power absorbed in the first transit through the plasma. No consistent attempt to determine the ultimate fate of the power which is not absorbed in the first transit is possible within the assumptions of the model: in particular both the antenna treatment and ray-tracing assume that no cavity eigenmodes are excited. Also, P_{COUPL} contains only the power radiated towards the plasma core, to the exclusion of the power possibly coupled to surface waves. Thus, η_{ABS} is not the same as the experimentally measured heating

efficiency, although it can be supposed to give a fair indication of the latter.

As already mentioned, the radiated electric field is decomposed in partial waves of the form

$$\vec{E}(\vec{r}) = \sum_{n_\varphi} \vec{E}_{n_\varphi}(\psi,\vartheta)\, e^{i\left(n_\varphi \varphi + \sigma_{n_\varphi}(\psi,\vartheta)\right)} \qquad (2)$$

On the one hand, this decomposition is essential to deal with the fact that the antennas are much shorter than the wavelength in the toroidal direction: ray tracing and power transport can only be implemented separately to each partial wave, which is uniform in φ /5/. On the other hand, to a rough approximation, the decomposion according to n_φ is also a decomposition with respect to $k_{//}$, the component of the wavevector parallel to the static magnetic field; hence the value of n_φ determines the intensity of ion cyclotron and electron trnasit time damping, or wether the wave will suffer mode conversion on incidence on a wave resonance or not. In other words, the decomposition (2) is also very useful to understand the role of the various heating mechanisms, and the effects of modifying the antenna in order to shape the spectrum.

All ICH methods are known to produce supratermal anisotropic ion populations, particularly in the case of low minority concentrations. Expressions for the effective temperature T_{eff} and density n_{eff} of these tails, obtained by balancing quasilinear and collisional diffusion in velocity space, can be found in the literature /6/, and can be easily used in connection with the RAYIC code /7/. Nevertheless in this work we have restricted ourselves to simulate these tails in a few cases with

arbitrarily chosen values of T_{eff} and n_{eff}, for two reasons. In the first place, the selfconsistent evaluations of the quasilinear distribution functions require the knowledge of the local electric field E_o at each point. Although E_o can in principle obtained by performing explicitly the superposition (2) of all partial waves, this task would consume an excessive amount of computer time and storage (analytic estimates of E_o cannot give more than an order of magnitude). Even if the problem of evaluating E_o could be solved, a selfconsistent evaluation of T_{eff} and n_{eff} would make sense only if the plasma parameter, particularly the temperature, where themselves evaluated consistently with the heating input, for example using a transport code.

RAYIC is so organized thad it can be coupled with such a code without difficulty /1/: in particular, for each run, it evaluates the power deposition profiles for each species of particles, to be used as power source in a transport code. A few examples of these profiles will be presented below; in all case, absorption is well localized in the central region of the plasma, typically $\psi \lesssim 0.3$. For this study, hovever, RAYIC has been used as an independent program.

2 - He_3^{++} MINORITY IN AN HYDROGEN PLASMA.

This heating scheme can be of temporary interest in JET, to postpone routine work with Deuterium as majority species, which might give rise to contamination problems. It presents the unfavorable property that an evanescent layer screens the cyclotron resonance of the minority species for waves incident from the LMFS.

An example of dispersion curves near resonance is given in Fig. 3. From their behaviour, it can be deduced that the ion-ion hybrid resonance can in this case be adequately treated in the cold plasma approximation; it is then a particular case of the Budden tunneling problem /8/-/9/. For LMFS incidence, the coefficients of reflection, transmission and absorption in the mode conversion regime are found to be: /3/

$$R = (1 - e^{-\eta_1})^2 \qquad T = e^{-2\eta_1} \tag{3}$$

$$A = e^{-2\eta_1}(1 - e^{-2\eta_1})$$

where

$$\eta_1 = \frac{\pi}{18}\frac{\omega_{pH}}{c} R_T \frac{n_{He_3^{++}}/n_e}{|\cos\psi|} \tag{4}$$

is the effective optical thickness of the cut off-resonance layer. ω_{pH} is the ion plasma frequency of the hydrogen plasma, R_T is the distance of the cyclotron resonance of the minority ions, $\omega = \Omega_{He_3}$, from the vertical axis, and

$$\psi = \operatorname{atan} k_z/k_x \tag{5}$$

The factor $|\cos\psi|^{-1}$ takes into account the fact that for obliquely incident wavefronts, $k_z \neq 0$, the reflection caustics move away from the $L = 0$ perpendicular cut off, thereby enlarging the evanescence layer.

A more detailed analysis /10/ shows that in this regime the absorbed power is coupled to the torsional Alfven wave, which in turn is easily absorbed by the electrons. Direct cyclotron damping of the compressional wave by the minority ions is quite weak,

$$(6) \qquad \frac{\Delta P_X}{P_X} \cong 0{,}24\pi \frac{\omega_{pH} R_T}{c} \frac{n_e/n_{He_3}}{|\cos\psi|} \cdot n_{//}^2 \frac{\omega_{pH}^2}{\Omega_{cH}^2} \cdot \frac{v_{th\,He_3}^2}{c^2}$$

where $P_X = T \cdot P_{coupl}$ is the trasmitted power flux, and $v_{th_\alpha}^2 = 2T_\alpha/m_\alpha$. The linear dependence of ΔP_X on the minority temperature and its inverse dependence on the minority concentration is easily explained by the screening of the left-hand circularly polarized component of the wave electric field E_+ by the minority ions themselves.

These estimates hold if the ion-ion hybrid resonance is well outside the Doppler broadened cyclotron resonance of the He ions, a condition which can be written

$$(7) \qquad |k_{//}| \lesssim 1.3 \frac{B_0}{\sqrt{T_{He_3}}} \cdot \frac{100\, n_{He_3}}{n_e}$$

(B_0 in Tesla, T_{He_3} in Kev, $k_{//}$ in m^{-1}). In the minority regime, when this inequality is reversed, screening of E_+ is only partial, and direct IC absorbtion by He_3^{++} ions is much more efficient, is proportional to the minority concentration and independent from the temperature. At the same time wave conversion is suppressed. In this case one finds:

$$(8) \qquad \frac{\Delta P_X}{P_X} \cong 1 - e^{-2\eta_1} \cong 2\eta_1$$

where $P_\chi = P_{coupl.}$ This result can be interpreted as stating that in the minority regime the transmission coefficient has still the form (3), but all the missing power is now absorbed by the minority ions.

Since the $k_{//}$-spectrum incident on the resonance layer is always very broad, condition (7) has to be interpreted as separating a low $k_{//}$ portion, absorbed mainly by the electrons, from a high $k_{//}$ portion absorbed mainly by the minority ions. For efficient electron heating, η_1 should be close to the value $\ln(2)/2 \cong 0.347$ which maximizes A in Eq. (3). From Eqs. (6) and (8) on the other hand it follows that direct ion heating is most efficient just around the transition between the minority and the mode-conversion regimes. Both these considerations lead to the conclusion that in large devices of the size of JET efficient heating by this scheme requires a rather precise control of the minority concentration.

This is confirmed by Fig. 4a, which shows the first transit absorption for the standard target plasma as a function of the He_3^{++} concentration. For these parameters, the optimum value of η_1 occurs at a He concentration of about 5%; above this concentration most of the power is reflected back from the cut off, and electron heating decreases. Already well before this concentration, hovewer, the portion of the specrum in the minority regime and leading to direct ion heating decreases sharply.

Fig. 4b shows the same curves assuming that the a suprathermal population of He_3 ions has been generated (20% of the He_3^{++} ions are assumed to have a temperature of 17 Kev). The transition value of $k_{//}$ is thereby decreased by almost a factor of 3, resulting in a marked reduction of electron heating in favour of ion heating. In this case therefore the minority concentration is appreciably less critical than for a maxvellian

distribution.

An interesting feature of Fig. 4 is that the electron absorption does not vanish at zero He_3^{++} concentration. The modest ($\sim$2%) residual damping is due to electron Transit Time damping; the corresponding power deposition profile is shown in Fig. 5.

Fig. 6 compares the power deposition profiles for two He_3^{++} concentrations (no suprathermal ions are assumed): $n_{He_3}/n_e = 0.015$, close to the optimum for IC damping, and $n_{He_3}/n_e = 0.03$, close to the optimum for electron damping.

Fig. 7 presents the power balance as a function of the toroidal wave number n_φ, again for a few different concentrations. As n_{He_3}/n_e increases, the transition between dominant absorption by the electrons and dominant absorption by the ions moves to higher values of n_φ, as expected from the previous discussion. Above $n_{He_3}/n_e = 0.015$, direct IC damping still increases with He_3^{++} concentration only for modes with quite large values of n_φ, to which little power is coupled by the antenna.

Fig. 8 shows the density dependence of the single transit absorption at the fixed minority concentration of 2%. The optimum minority concentration is a decreasing function of the total density, and equals 2% at $n_e = 5.10^{13}$. Thus η_{ABS} first increases with n_e, then saturates as n_e exceeds the mentioned value.

The temperature dependence of η_{ABS} is shown in Fig. 9. As expected, direct minority heating first increases rapidly with T at the expense of electron heating. At T $\simeq$ 3 Kev, however, all partial waves but the one with $n_\varphi = 0$ are already in the minority regime. Above this temperature ion

absorption saturates at a value roughly specified by Eq. (8). At still higher temperatures, $T \gtrsim 5$ Kev, nonlocalized Transit Time absorption by the electrons begins to play a nonnegligible role, and electron absorption is seen to increase again.

Fig. 10 illustrates the effect of varying the applied frequency, at a He_3^{++} concentration of 2%. The position of the He_3^{++} cyclotron resonance moves from the outer plasma edge at f=25 Mhz, to the inner edge at f = 50 Mhz; above f = 40 Mhz, moreover, the fundamental resonance of the hydrogen ions appears near the outer edge. The power absorption by the hydrogen first increases, as the density near $\omega = \Omega_H$ is low, then decreasees again due to the well-known screening effect at larger densities. The power absorbed by the minority ions also decreases sharply above 40 Mhz. This is partly due to the different shape of wavefronts in the resonance regions: Figs. 11 and 12 show the wavefronts of the n_φ = Omodes at f = 35 Mhz and f = 50 Mhz, respectively.

The fact that modes with different n_φ can be in different absorption regimes suggests the possibility of controlling the absorption efficiency by shaping the launched spectrum. Exciting the four antennas with different phases has a negligible influence on the specrum, since the maximum achievable displacement is much smaller than the width of the spectrum of a single antenna. The simplest method is to vary the toroidal width D of each antenna. Increasing D makes the spectrum narrower, thus favoring electron heating, as confirmed by Fig. 13.

A more interesting method is to use quadrupole antennas, i.e. antenna consisting of two symmetric halfs, in each of wich the current flows in opposite direction /7/. The spectrum launced by four such antennas is

shown in Fig. 14, together with the power balance resolved for n_φ for a He_3^{++} concentration of 2%. The effect of the spectrum modificationon on the concentration dependence of the first transit absorption is shown in Fig. 15. Compared to the case of a dipole antenna, Fig. 3a, the width of the ion curve is only sligtly broadened; the absolute values of η_{ABS} are however multiplied by almost a factor of 1.5, while optimum electron heating is pushed to higher concentration and depressed in absolute value.

To conclude this section, we show in Fig. 16 the single transit absorption efficiency for the case of a He_3^{++} minority in a Deuterium plasma, again for standard conditions. The most obvious difference between Deuterium and Hydrogen as bulk plasma is that in the case of Deuterium the cyclotron resonance of the He_3^{++} ions lies to the LMFS of the ion-ion hybrid resonance. Also, for a given electron density and minority concentration, the effective optical thickness η_+ is reduced by a factor of $\sqrt{2}$. These two circumstances together make the concentration of He_3^{++} much less critical than in the previous case. Nevertheless, as soon as a wave enters the mode conversion regime, this favorable configuration is increasingly spoiled by efficient screening of E_+ by the minority ions. Thus even in this case, η_{ABS} saturates and decreases again slowly as n_{He_3}/n_e exceeds about 0.05.

3 - FIRST HARMONIC HEATING OF A DEUTERIUM PLASMA

An example of dispersion curves near the first harmonic resonance of a Deuterium plasma is shown in Fig. 17. The existence of an evanescence region for small $k_{//}$ between the $\omega = 2\Omega_{cD}$ resonance and the confluence with the Bernstein wave has been pointed out by Weynants /11/. The effective optical thickness of this layer is

$$\eta_2 = \frac{\pi}{4} \frac{\omega_{pD}}{c} R_T \frac{\beta_i}{|\cos\psi|} \tag{9}$$

where

$$\beta_i = \frac{\omega_{pD}^2}{\Omega_{cD}^2} \cdot \frac{v_{thD}^2}{c^2} \cong \frac{4\pi n_e T_D}{B_0^2} \tag{10}$$

As long as Doppler broadening of the $\omega = 2\Omega_{cD}$ resonance is insufficient to eliminate the evanescent layer, the coefficients of reflection, transmission and coupling to the Bernstein wave, for a compressional wave incident from the LMFS, are

$$T_F = e^{-2\eta_2} \qquad R_F = (1 - e^{-2\eta_2})^2$$

$$T_B = e^{-2\eta_2}(1 - e^{-2\eta_2}) \tag{12}$$

The Bernstein wave propagates away from the resonance, and is therefore easily absorbd by the electrons. By analogy with ion-ion hybrid resonances, we will call this regime mode-conversion regime.

A peculiar feature of the evanescence layer is that its physical thickness,

$$\Delta X \cong \frac{\pi}{8} \beta_i R_T \tag{13}$$

is proportional to the product $n_i T$. Since the thickness of the Doppler broadened cyclotron harmonic resonance increases only as $\sqrt{T}$, this has the unexpected consequence that the portion of the coupled spectrum which is in the mode conversion regime extends to higher toroidal modes not only when the density increases, but also when the temperature increases:

$$(14) \qquad |n_{//}| \frac{V_{thD}}{c} \lesssim \frac{\pi}{8} \beta_i$$

or, for wavefronts not too obliquely incident,

$$(14') \qquad |n_\varphi| \lesssim \frac{\pi}{4} \frac{\omega_{pi}^2}{\Omega_{ci}^2} \frac{V_{th}}{c} \cdot \left(\frac{\omega}{c} R_T\right)$$

Thus increasing $n_e\sqrt{T}$ first favours electron heating. Of course, if η_2 increases above about 0.347, coupling to Bernstein waves will decrease, and first pass absorption efficiency will saturate, at least until electron Transit Time damping takes over. This effect can be partly counteracted by shaping the n_φ spectrum. We also recall that in the mode conversion regime direct absorption by Deuteriumis proportional to $n_{//}^2 \beta_i$, while for larger values of n_φ it becomes proportional to the much larger factor $n_\perp^2 \beta_i$

The dependence of η_{ABS} on density and temperature is illustrated in Figs. 18 and 19 respectively. It is in good agreement with the previous discussion, considering that η_2 is about optimum at $n_e = 5.10$ and $T_D = 4$ Kev. Electron Transit Time absorption can be seen to play a role starting from $T_e \simeq 5$ Kev: an idea of its importance can be gained from Fig. 20, which shows how the transported power flux decreases along rays for the partial wave $n_\varphi = 20$ at $T_e = 8$ Kev. Only about 80% of the coupled flux reaches the resonance layer, about six wavelengths away from the antenna; the effect is stronger for rays near the equatorial plane, which traverse

regions of higher electron density and temperature.

Details of the n_φ repartition of the coupled and absorbed power are shown in Fig. 21 for two different temperatures. The transition from mode conversion to cyclotron harmonic damping occurs near $n_\varphi = 8$ at $T_D = 1.7$ Kev, near $n_\varphi = 16$ at $T_D = 8$ Kev, in agreement with the $T^{1/2}$ dependence predicted by Eq. (14). Fig. 22 finally shows the power deposition profiles for the same two situations.

4 - H^+ MINORITY IN A DEUTERIUM PLASMA

An example of dispersion curves in this case is shown in Fig. 23. As n_{H^+}/n_e increases, the evanescence layer moves away from the $\omega = \Omega_H = 2\Omega_D$ resonance, and its effective optical thickness increases:

(15) $$\eta = \eta_1 + \eta_2$$

where η_2 is still given by Eq. (9), while the contribution of the minority ions is

(16) $$\eta_1 = \frac{\pi}{4} \frac{\omega}{c} P D R_T \frac{n_H/n_e}{|\cos\psi|}$$

In the mode conversion regime transmission, reflection and coupling to the Bernstein wave are described again by Budden like formulae, which for LMFS incidence are

(16) $$T_F = e^{-2\eta} \qquad R_F = (1-e^{-2\eta})^2$$

$$T_B = e^{-2\eta}(1-e^{-2\eta})$$

The power coupled to the Bernstein wave is expected, as before, to finally heat the electrons.

For JET parameters, η_1 easily exceeds η_2 by an appreciable factor ($\eta_1 \cong \eta_2$ already for $n_H/n_e = 0.005$ at $n_e = 5.10^{13}$ and $T_H = 2$ Kev), and becomes larger than unity at reasonable H^+ concentrations. Under this conditions, a wave will be mode converted at the ion ion hybrid resonance if

$$(17) \qquad |n_{//}| \frac{v_{th}}{c} \lesssim \frac{3}{8} \frac{n_H}{n_e}$$

In the mode conversion regime direct IC heating of the H^+ ions is reduced by the screening of the E_+ component of the electric field:

$$(18) \qquad \frac{\Delta P_X}{P_X} \cong \pi \frac{\omega_{PD}}{c} R_T \frac{n_e/n_H}{|\cos\psi|} \cdot n_{//}^2 \frac{\omega_{PD}^2}{\Omega_{CD}^2} \frac{v_{th\,H}^2}{c^2}$$

This equation is similar to Eq. (6), and has the same explanation. Nevertheless, IC damping by H^+ is relatively efficient even in this regime, and exceeds by far damping by D^+ and electrons at all concentrations. First harmonic heating of D^+ ions is reduced by screening of E_+ due to the minority ions, and therefore becomes a second order effect in the temperature when inequality (17) is satisfied. Electron heating is also a rapidly decreasing function of the H^+ concentration, due to the large values of η_1, which reduces tunneling to the Bernstein wave beyond the evanescence layer.

All these trends can be recognized in Fig. 24, which shows the single transit absorption efficiency in the standard target plasma as a function of n_H/n_e. For these parameters, coupling to Bernstein waves is optimum at a concentration of 1%; for such low concentrations however, only the partial wave with $n_\varphi = 0$ satisfies condition (18), so that the amount of

power transferred to the electrons remains quite modest. For larger concentrations, the fraction of the spectrum which suffers mode conversion increases, but η_1 becomes too large for efficient electron heating.First harmonic heating of Deuterium also becomes rapidly negligible. On the other hand, direct IC heating of H^+ ions has a broad maximum around 3% to 5% concentration, and decreases only slowly at higher concentrations, as more partial waves enter the mode conversion regime. The effect of screening in this regime is to be seen in Fig. 25, in which the fraction of power absorbed by H^+ is shown versus n_ϕ for a low and a high minority concentration: while this fraction increases with concentration for large values of n_ϕ, it is appreciably reduced for low to medium values which satisfy the condition for mode conversion.

The absorption efficiency is enhanced if the minority temperature increases above that of the bulk plasma, as shown in Fig. 26b. A further enhancment can be obtained by using a quadrupole antenna, which couples poorly to low n_ϕ values (Fig. 26c) In both these cases, electron heating is futher reduced compared to Fig. 24.

Fig. 27 shows the dependence of the absorption efficiency on density. Absorption by H^+ increases with density both in the mode conversion and in the minority regime, although it is weaker in the former case. While the monotonic increase of absorption by Deuterium does not need explanation, the increase of electron heating at high densities, $n_e \gtrsim 6.10^{13}$, is mainly attributable to Transit Time damping. Both D^+ and electron heating remain quite small throughout.

Fig. 28 illustrates the dependence of η_{ABS} on the central temperature. After an initial steep rise, absorption by H^+ saturates and even

decreases, while absorption by D^+ and electrons continues to increase. Above 5 kev, the downshift of the transition between mode conversion and minority regimes is more than compensated by the increase of Transit Time and D^+ first harmonic damping, which compete with IC of H^+ in the upper part of the spectrum. The role of Transit Time damping at T_e = 8 Kev can be seen in Fig. 29: the electron power absorption profile extends well beyond the resonance region; the H^+ and D^+ absorption profiles are slightly broadened, and the balance is shifted somewhat in favour of D^+. Fig. 30 shows the same effects in terms of the n_φ spectrum: at high temperatures the portion efficiently absorbed by H^+ shifts to lower values, while for $n_\varphi \gtrsim 20$ electrons and D^+ ions begin to absorb a nonnegligible fraction of the coupled power.

Note that in this part of the spectrum the first transit absorption is practically complete: this suggests that a further improvement of the global efficiency can be achieved by using quadrupole antennas. This is confirmed by Fig. 31, which shows that in this case practically all the coupled power is absorbed in a single transit as soon as T_e exceeds about 2 Kev. Note that electron and D^+ heating are also appreciable in this case, albeit much smaller than H^+ heating. Fig. 32 shows the power balance versus n_φ in this case.

5 - CONCLUSIONS.

With the help of the numerical code RAYIC we have explored in some details three IC heating scenarios for the JET plasma. The usefulness of the code in understanding the physics of heating is well confirmed, inspite of the limitations mentioned in the introduction.

All three methods have been found to be satisfactorily efficient. He_3^{++} minority in an Hydrogen plasma requires a rather precise control of the minority concentration, particularly if heating through the ion channel is wished. In the case of H^+ in a deuterium plasma, the large dimensions of the JET plasma make electron heating much less efficient than in smaller machines; the optimum H^+ concentration is also somewhat lower than what would be expected in small Tokamaks.

Use of quadrupole antennas apperars to enhance the absorption efficiency considerably. In the case of H^+ in a Deuterium plasma, total absorption in a single transit can already be achieved for such antennae at ohmically attainable temperatures.

Further devlopment of these investigations should include coupling the RAYIC code to a tokamak transport code, and the selfconsistent determination of the ion distribution functions from quasilinear theory.

REFERENCES

/1/ M. BRAMBILLA - RAYIC, a numerical code for the study of Ion Cyclotron Heating of Tokamak plasmas, Report IPP 4/216, February 1984.

/2/ M. BRAMBILLA - Ray tracing of Ion Cyclotron waves in Tokamak plasmas, Report IPP 4/210, March 1983.

/3/ M. BRAMBILLA, M. OTTAVIANI - Two Ion Hybrid resonances and Cyclotron absorption in Tokamak plasmas, Report IPP 4/212, November 1983.

/4/ P. REBUT - Proc 3d Int. Symp. on Heating in toroidal plasmas, Grenoble 1982, Vol. 3 p. 989.

/5/ M. BRAMBILLA, A. CARDINALI - Plasma Physics 24 (1982) 1187.

/6/ T. H. STIX - Nucl. Fusion 15 (1975) 737.

/7/ P. LALLIA, W.H.M. CLARK, J. JACQUINOT, F. SAND - Proc 4th Int. Symp. on Heating in toroidal plasmas, Rome 1984, paper C 21.

/8/ K.G. BUDDEN, Radio waves in the ionosphere, Cambridge Univ. Press 1961, Ch. 21.

/9/ Y. LAPIERRE - J. Plasma Phys. 29 (1983) 223.

/10/ M. BRAMBILLA, M. OTTAVIANI - to be published.

/11/ R.R. WEYNANTS - Phys. Rev. Lett. 33 (1974) 78.

TABLE I - STANDARD PLASMA PARAMETERS

Toroidal radius	R = 3 m.
Plasma radius	a = 0.4 m.
Shift of the magnetic axis	Δ = 0.28 m.
Magnetic field (at the centre of the vessel)	B = 3.45 T.
Toroidal current	I = 5 MA
Safety factor: on axis	q(0) = 1.13
Safety factor (at plasma edge)	q(a) = 3.77
Central electron density	$n_e(0) = 5\ 10^{13}\ cm^{-3}$
Central temperature (all species)	T(0) = 1.7 Kev.
Applied frequency: He_3^{++} in Hydrogen	f = 35 Mhz
First harm. of Deuterium	f = 50 Mhz
H^+ in Deuterium	f = 50 Mhz

TABLE II - ANTENNA PARAMETERS

Distance: antenna - wall	d_w = 0.1 m
antenna - plasma	d_p = 0.05 m.
Width of the antenna: dipole	D = 0.4 m.
quadrupole	D = 0.6 m.
Length of the antenna	h = 2x0.8 m.
Effective propagation constant	$\frac{\omega}{c}(L \cdot C)^{1/2} = 1.8$
N. of antennae along the torus	4
Relative phase between antennae	$\Delta\Phi = 180°$

FIGURE CAPTIONS

Fig. 1 - Meridian cross section of the JET MHD equilibrium.

Fig. 2 - Density, temperature and safety factor profiles.

a) He_3^{++} minority in a Hydrogen plasma.

Fig. 3 - Example of dispersion curves near the ion-ion hybrid resonance.

Fig. 4 - First transit absorption versus He_3^{++} concentration: a) standard plasma parameters; b) assuming that 20% of He_3^{++} has an effective temperature of 17 Kev.

Fig. 5 - Power deposition profile by electron Transit Time damping. Standard discharge parameters.

Fig. 6 - Power deposition profiles: a) $n_{He_3}/n_e = 0.015$; b) $n_{He_3}/n_e = 0.03$. Standard discharge parameters.

Fig. 7 - Spectral distribution of the coupled and absorbed power: a) $n_{He_3}/n_e = 0.005$; b) $n_{He_3}/n_e = 0.015$; c) $n_{He_3}/n_e = 0.03$. Standard discharge parameters.

Fig. 8 - First transit absorption versus density, $n_{He_3}/n_e = 0.02$, other parameters standard.

Fig. 9 - First transit absorption versus temperature, $n_{He_3}/n_e = 0.02$, other parameters standard.

Fig. 10 - First transit absorption versus applied frequency, $n_{He_3}/n_e = 0.02$, standard discharge parameters.

Fig. 11 - Rays and wavefronts of the $n_\varphi = 0$ partial wave at f = 35 Mhz.

Fig. 12 - Rays and wavefronts of the $n_\varphi = 0$ partial wave at f = 50 Mhz.

Fig. 13 - First transit absorption for different antenna widths (in the toroidal direction), $n_{He_3}/n_e = 0.02$, standard discharge parameters.

Fig. 14 First transit absorption for a quadrupole antenna versus He concentration. Standard discharge parameters.

Fig. 15 - Spectral distribution of the coupled and absorbed power for the quadrupole antenna, $n_{He_3}/n_e = 0.02$, standard discharge parameters.

Fig. 16 - First transit absorption in the case of He_3^{++} minority in Deuterium plasma. Standard discharge parameters.

b) First Harmonic Heating of a Deuterium plasma.

Fig. 17 - Dispersion curve for $k_{//} = 0$ near the first harmonic resonance of Deuterium.

Fig. 18 - First transit efficiency versus density. Other parameters standard.

Fig. 19 - First transit absorption versus temperature. Other parameters standard.

Fig. 20 - Power flux along the rays (the ascissa is the number of wavelengths from the first wavefront). T_e = 8 Kev, other parameters standard.

Fig. 21 - Spectral distribution of the coupled and absorbed power: a) T = 1.7 Kev; b) T_e = 8 Kev. Other parameters standard.

Fig. 22 - Power deposition profiles: a) T_e = 1.7 Kev; b) T_e = 8 Kev. Other parameters standard.

c) H^+ minority in a Deuterium Plasma.

Fig. 23 - Example of dispesion curves near the ion-ion hybrid resonance, H^+ minority in a Deuterium plasma.

Fig. 24 - First transit absorption versus H^+ concentration, standard discharge parameters.

Fig. 25 Spectral distribution of the coupled and absorbed power: a) n_H/n_e = 0.02; b) n_H/n_e = 0.1; other parameters standard. Only absorption by H^+ ions is shown.

Fig. 26 - First transit absorption versus H concentration: a) standard discharge parameters; b) T_H = 5.1 Kev, other parameters standard; c) quadrupole antenna, other parameters as in b). Only absorption by H^+ ions is shown.

Fig. 27 - First transit absorption versus density. n_H/n_e = 0.05, other parameters standard.

Fig. 28 - First transit absorption versus temperature. n_H/n_e = 0.05, other parameters standard.

Fig. 29 - Power deposition profiles, n_H/n_e = 0.05; a) T = 2 Kev; b) T = 8 Kev; other parameters standard.

Fig. 30 - Spectral distribution of the coupled and absorbed

power, n_H/n_e = 0.05; a) T = 2 Kev; b) T = 8 Kev. Other parameters standard.

Fig. 31 - First transit absorption versus central temperature for a quadrupole antenna. n_H/n_e = 0.05, discharge parameters standard.

Fig. 32 - Spectral distribution of the coupled and absorbed poser for a quadrupoleantenna, n_H/n_e = 0.05; a) T = 2 Kev, b) T = 8 Kev. Other parameters standard.

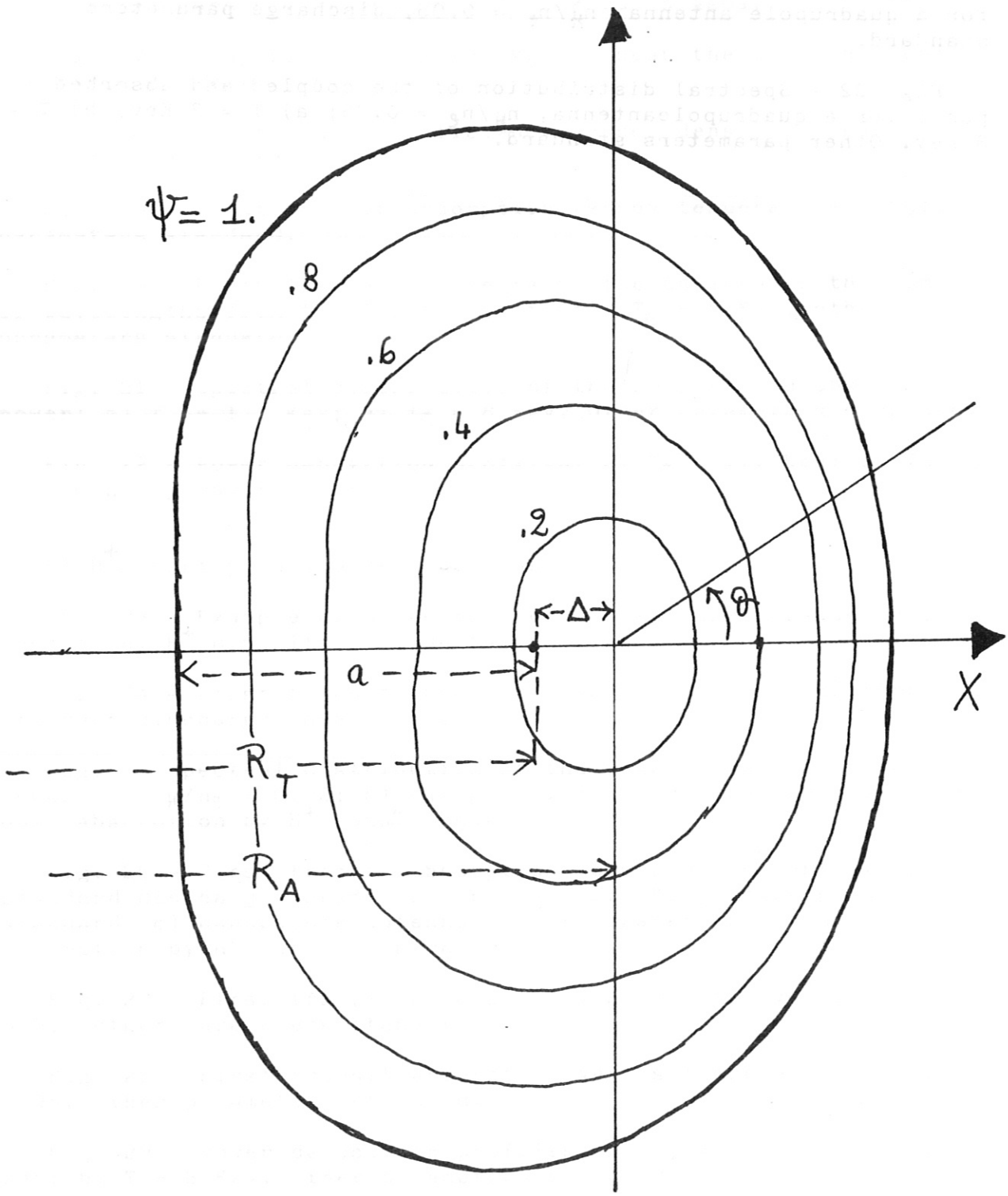

Fig. 1 - Jet MHD equilibrium
(meridian cross-section)

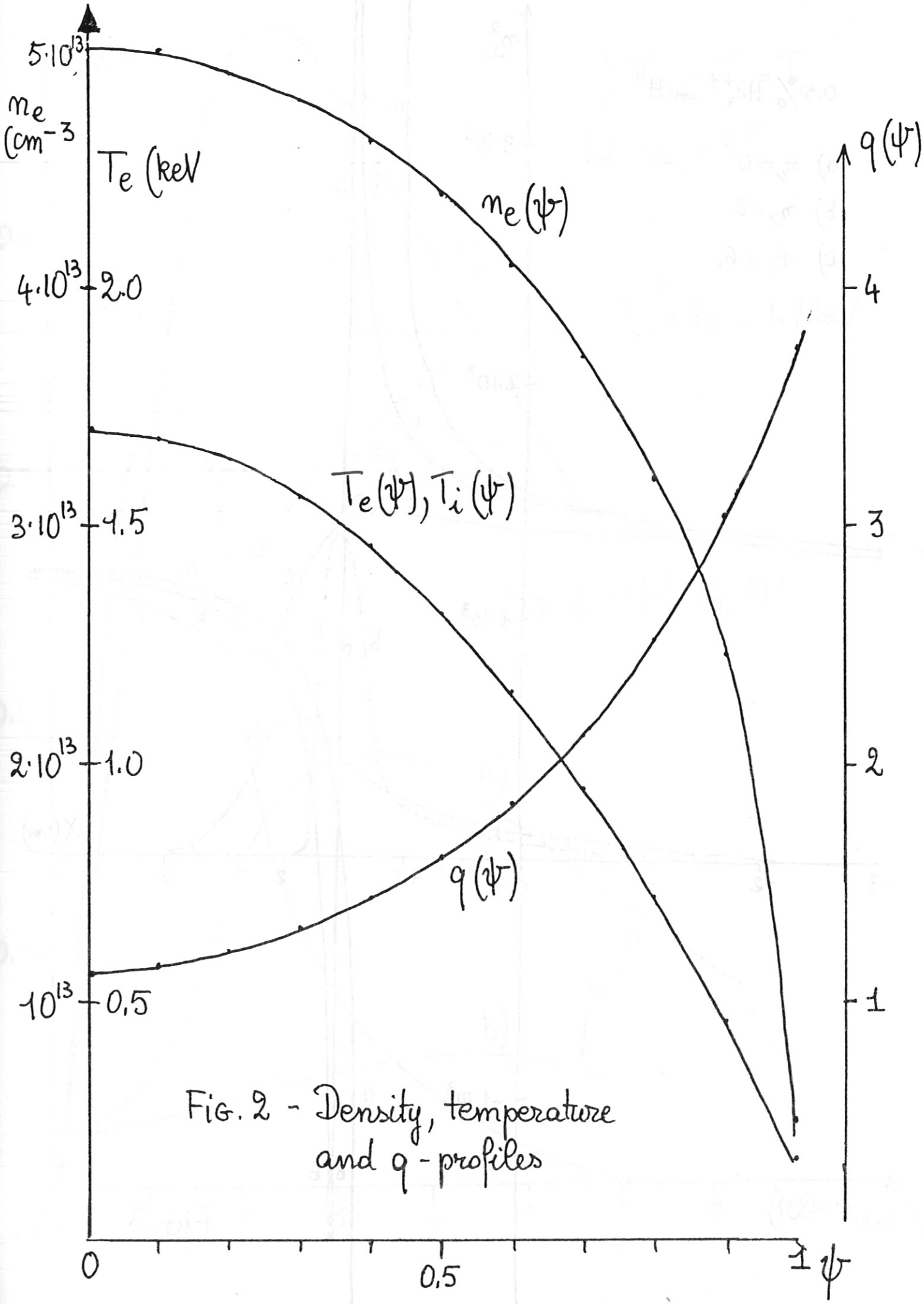

Fig. 2 - Density, temperature and q - profiles

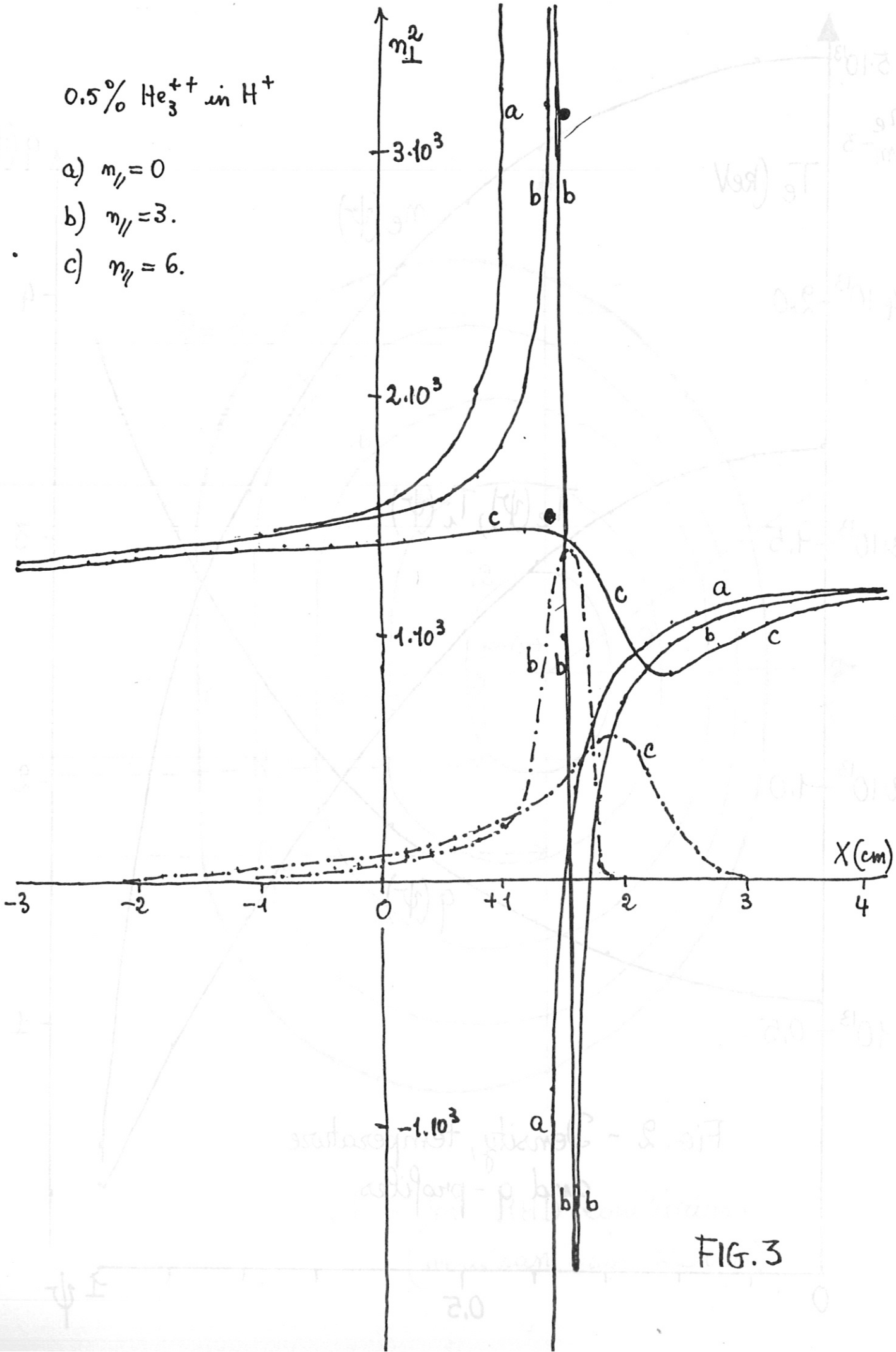
0.5% He_3^{++} in H^+
a) $n_{//} = 0$
b) $n_{//} = 3.$
c) $n_{//} = 6.$
$n_\perp^2$
3.10^3
2.10^3
1.10^3
-1.10^3
a
b
c
X(cm)
-3
-2
-1
0
+1
2
3
4

FIG. 3

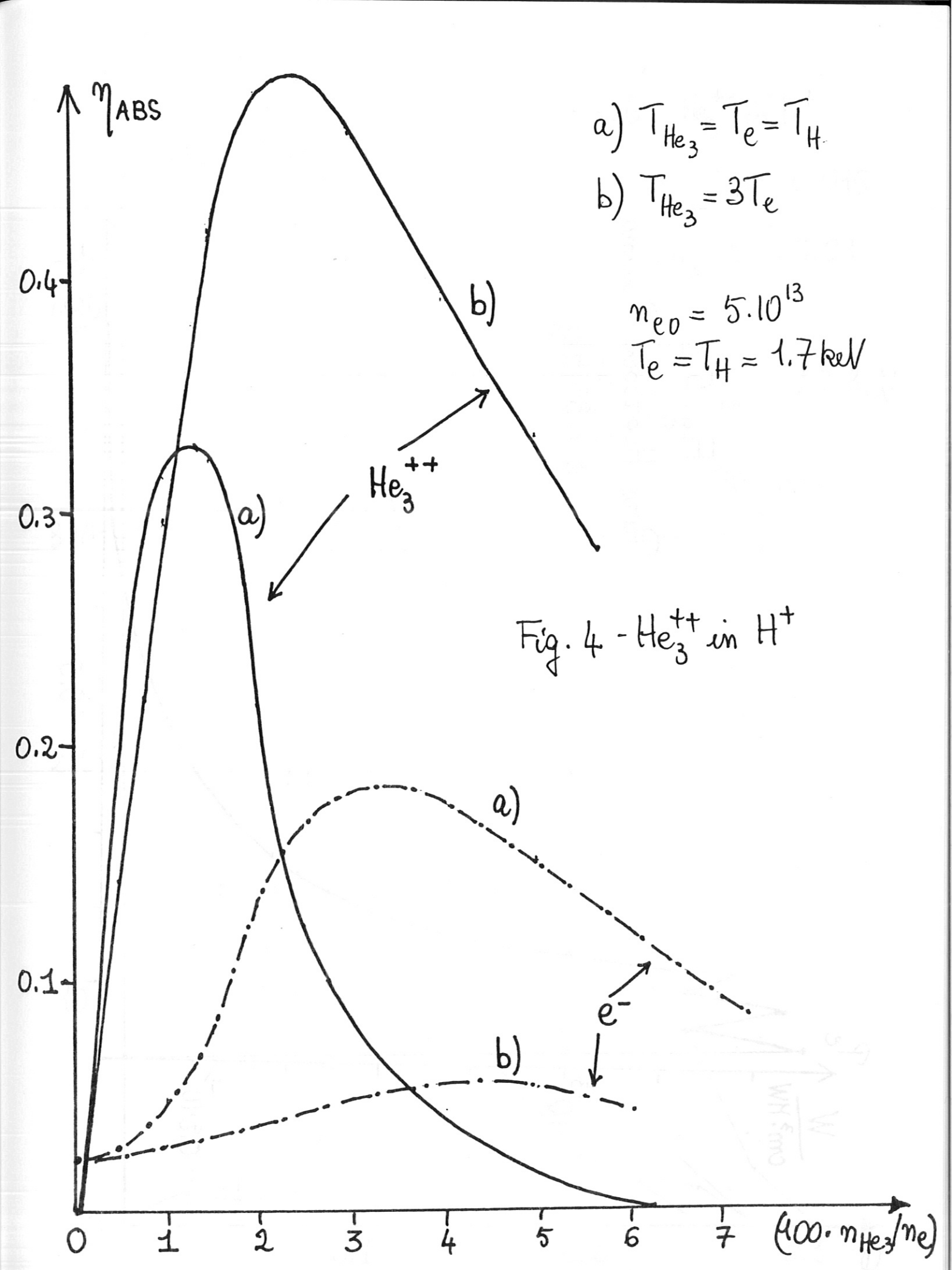
η_{ABS}
0.4
0.3
0.2
0.1
0
1
2
3
4
5
6
7
$(400 \cdot n_{He_3}/n_e)$
a) $T_{He_3} = T_e = T_H$
b) $T_{He_3} = 3T_e$
$n_{e0} = 5.10^{13}$
$T_e = T_H = 1.7\,keV$
He_3^{++}
a)
b)
a)
b)
e^-

Fig. 4 - He_3^{++} in H^+

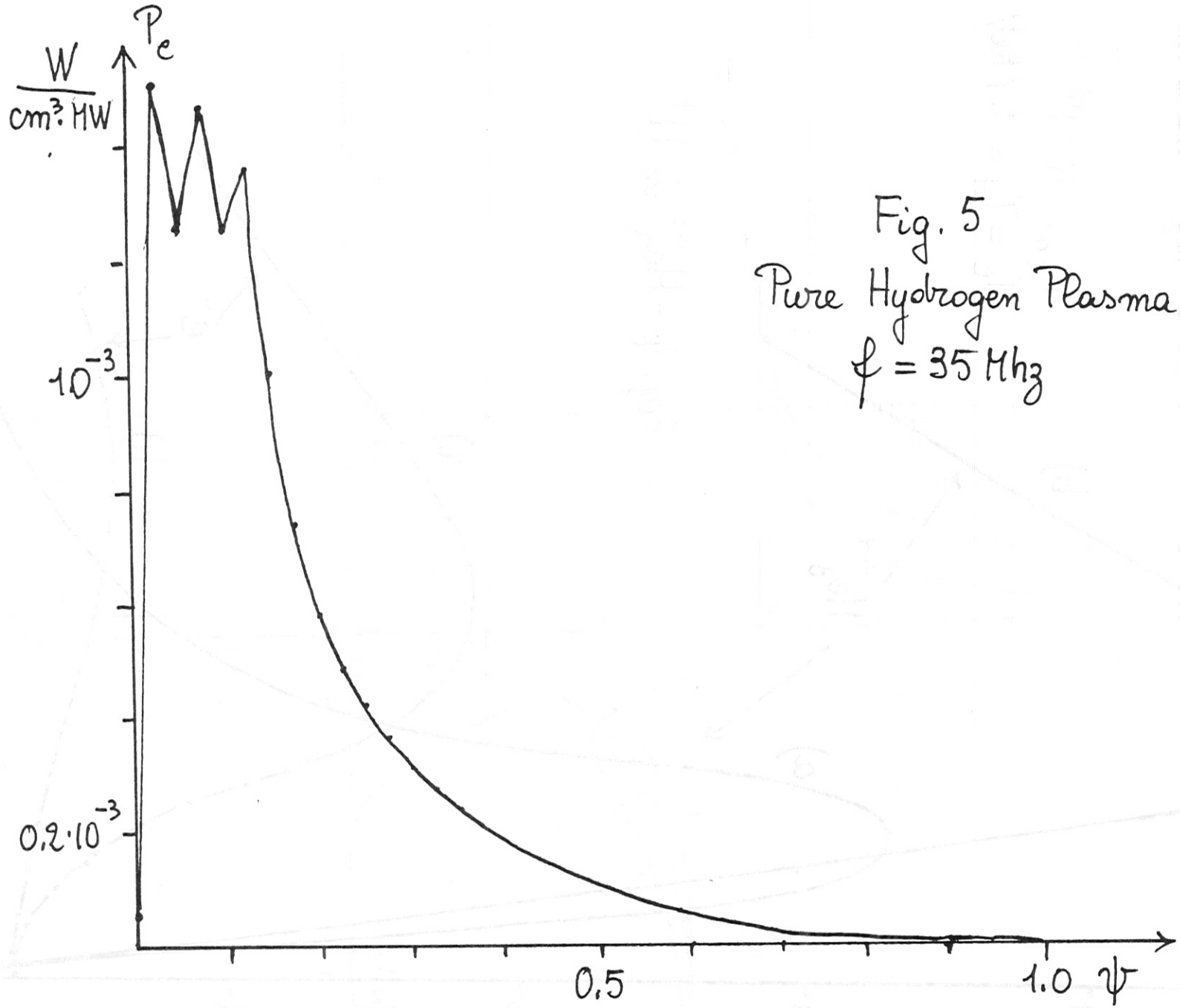

Fig. 5
Pure Hydrogen Plasma
$f = 35$ Mhz

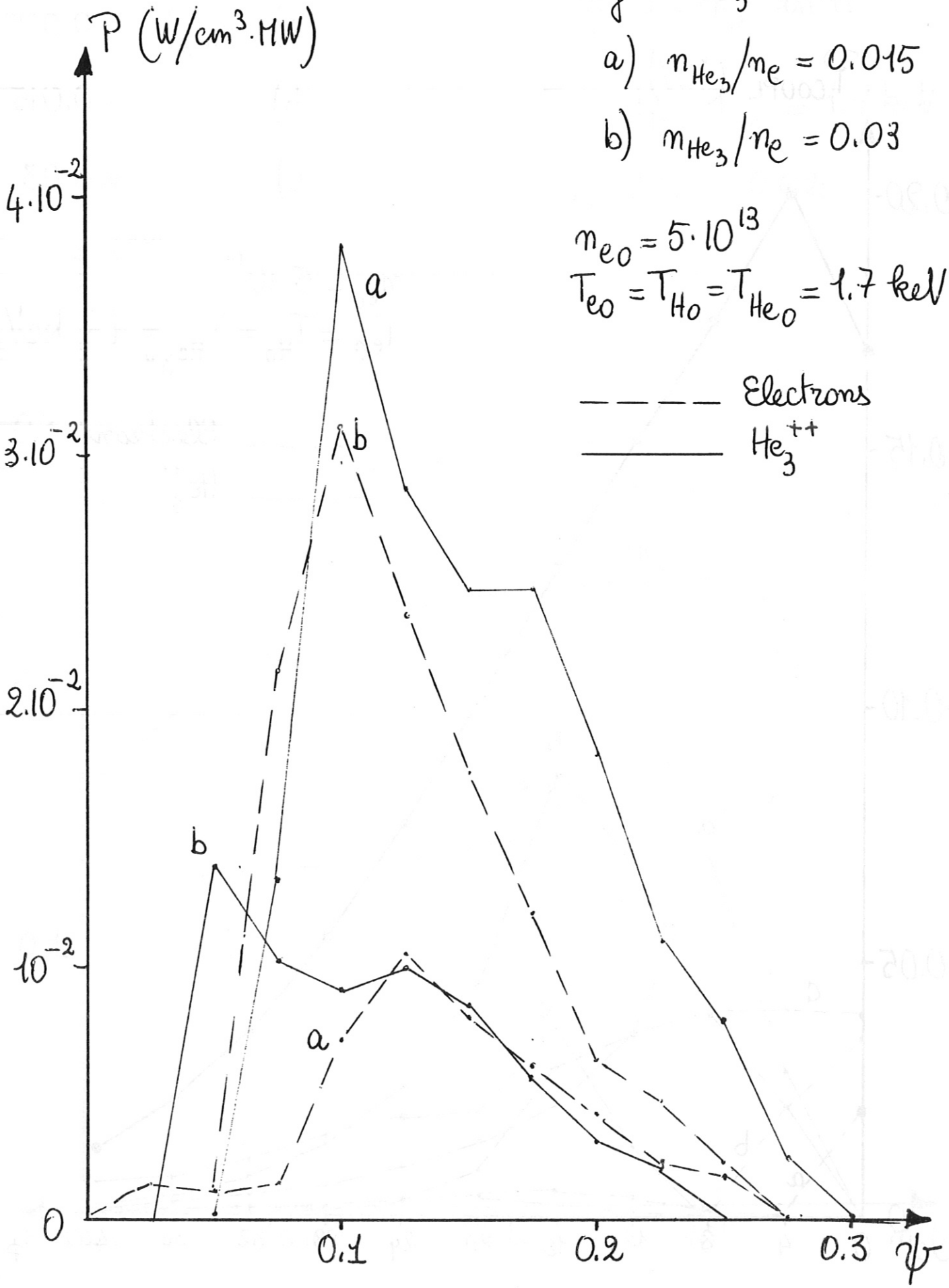

Fig. 6 He_3^{++} in H^+

a) $n_{He_3}/n_e = 0.015$

b) $n_{He_3}/n_e = 0.03$

$n_{e0} = 5 \cdot 10^{13}$

$T_{e0} = T_{H0} = T_{He0} = 1.7$ keV

– – – – Electrons

——— He_3^{++}

Fig. 7 He_3^{++} in H^+

a) $n_{He_3}/n_e = 0.005$

b) $= 0.015$

c) $= 0.03$

$n_{e0} = 5 \cdot 10^{13}$

$T_{e0} = T_{H0} = T_{He_3 0} = 1.7$ keV

----- Electrons

——— He_3^{++}

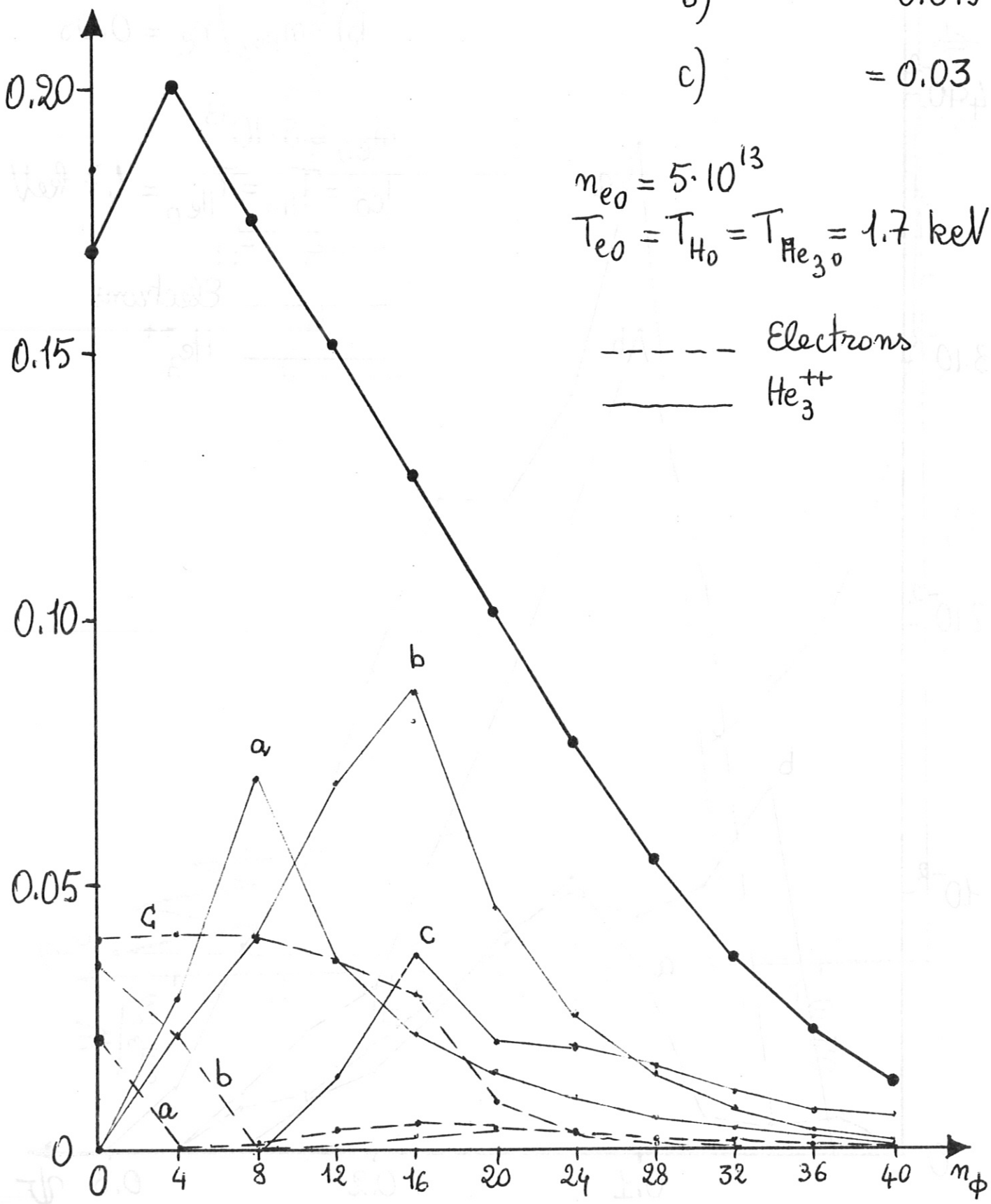

Fig. 8 He_3^{++} in H^+

$T_e = T_H = T_{He_3} = 1.7$ keV

$n_{He_3}/n_e = 0.02$

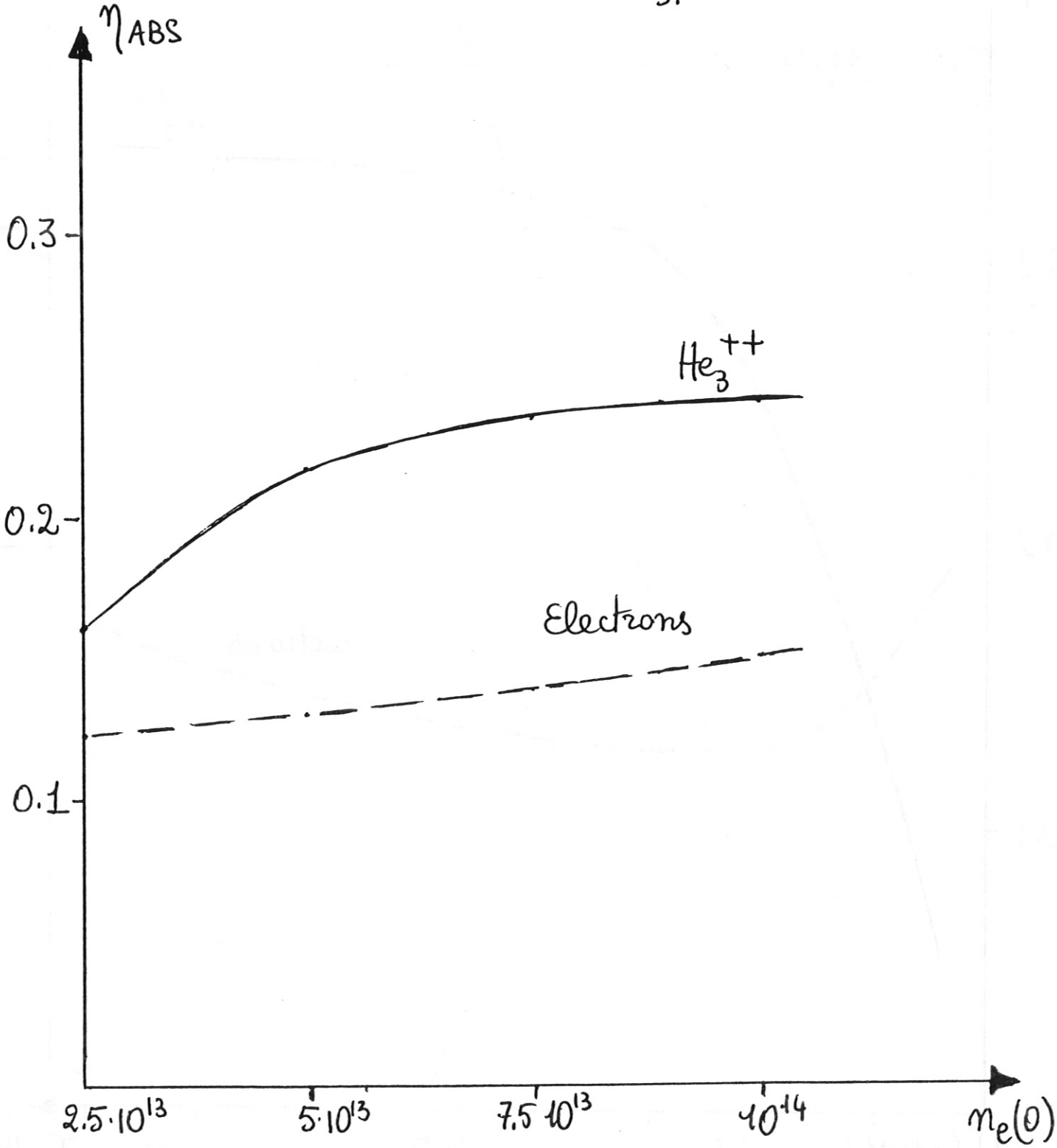

Fig. 9 He_3^{++} in D^+

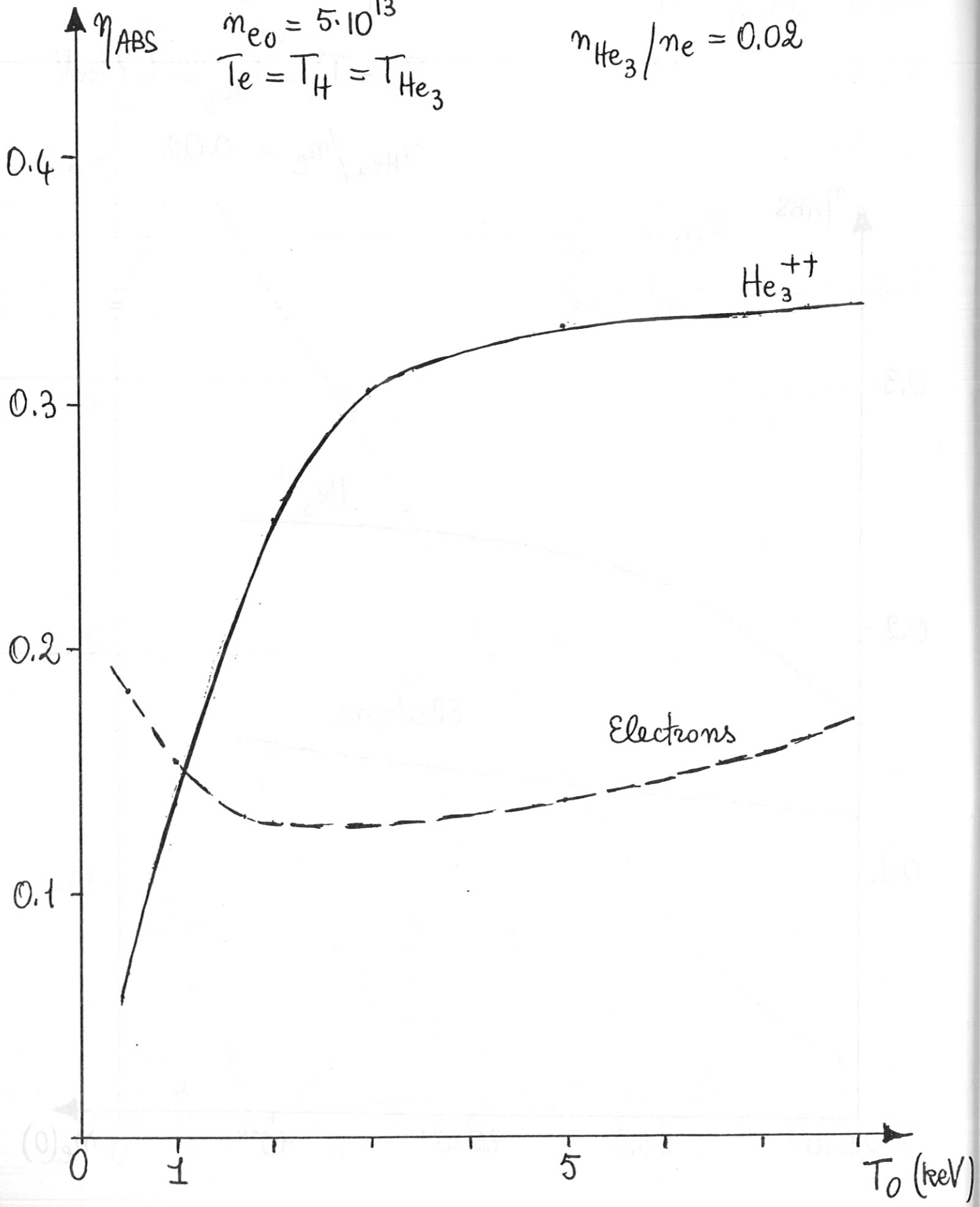
η_{ABS}
$n_{e0} = 5 \cdot 10^{13}$
$T_e = T_H = T_{He_3}$
$n_{He_3}/n_e = 0.02$
0.4
0.3
0.2
0.1
He_3^{++}
Electrons
0
1
5
T_0 (keV)

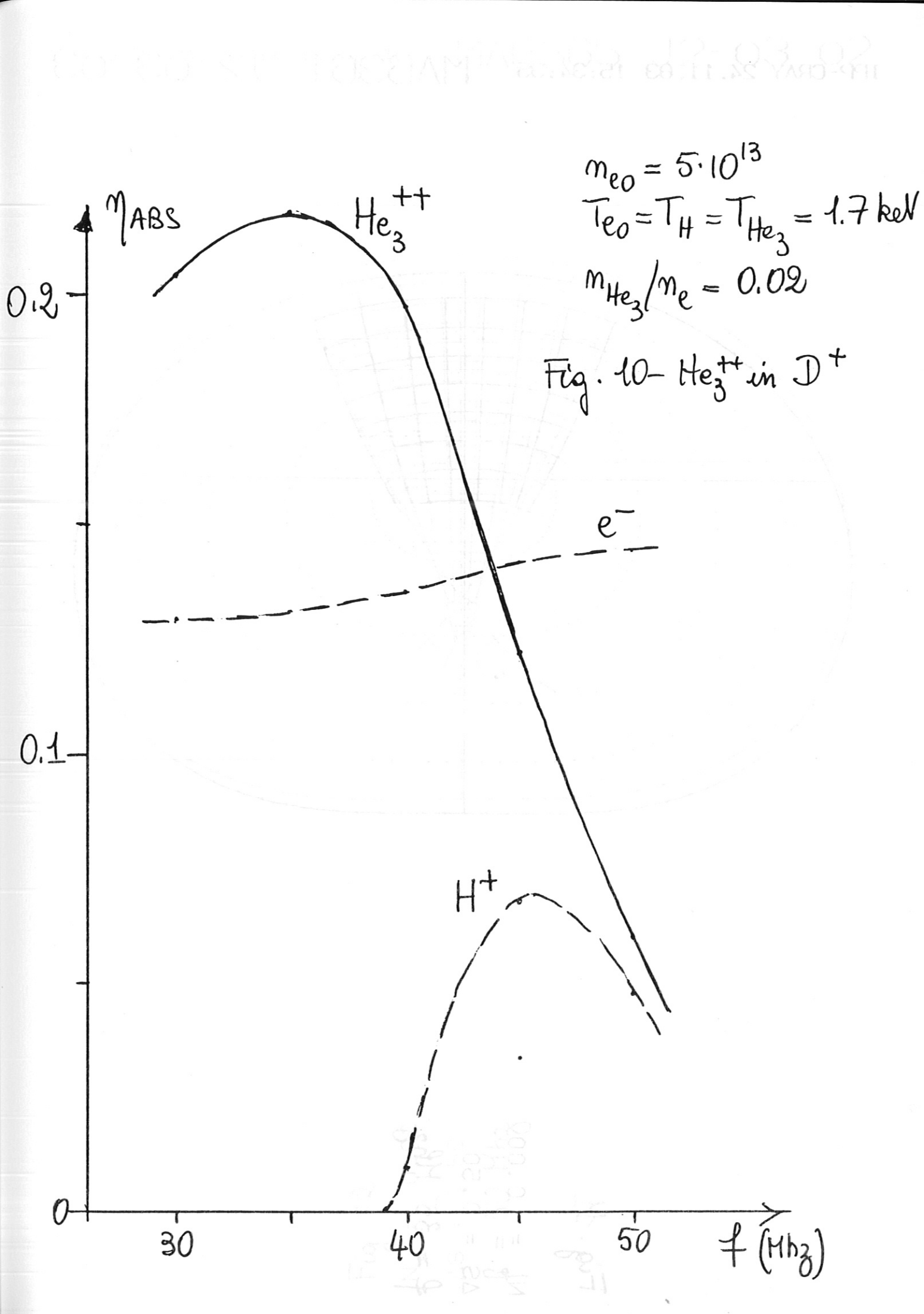

Fig. 10 – He_3^{++} in D^+

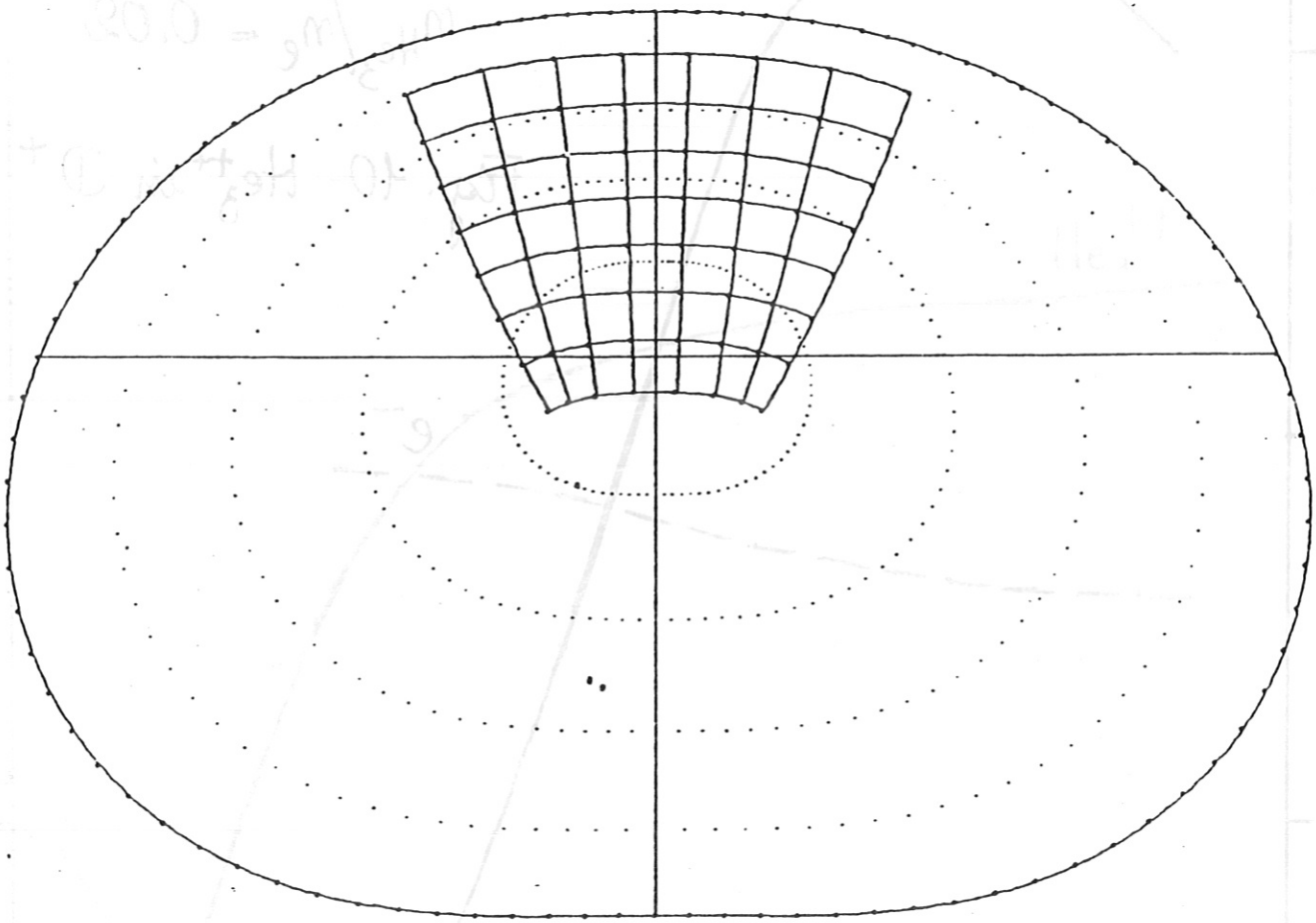

Fig. 11

N_ϕ = 0.00

ΔS = 0.50

f = 35 MHz

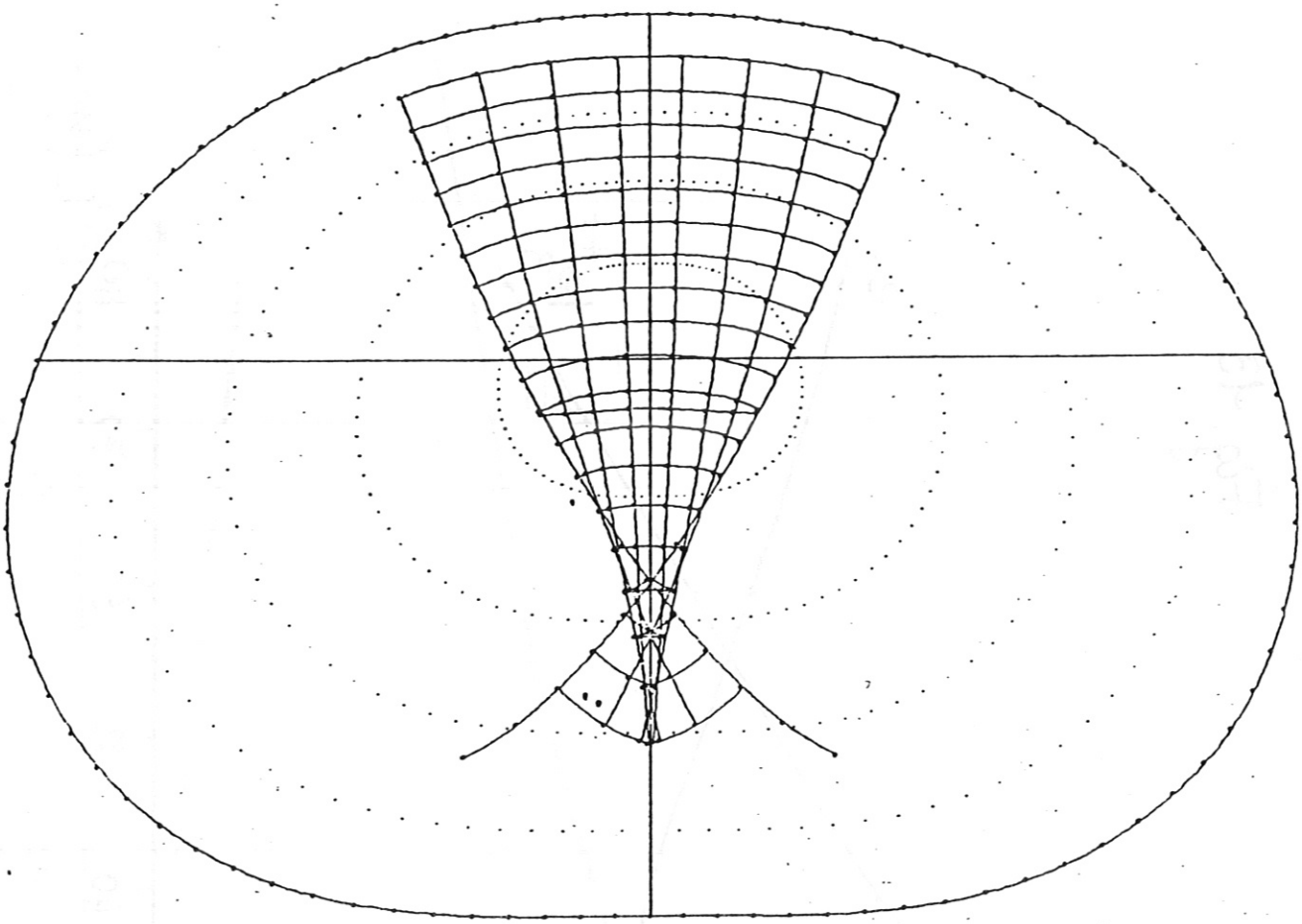

Fig. 12
N_ϕ = 0.00
ΔS = 0.50
f = 50 Mhz

Fig. 13

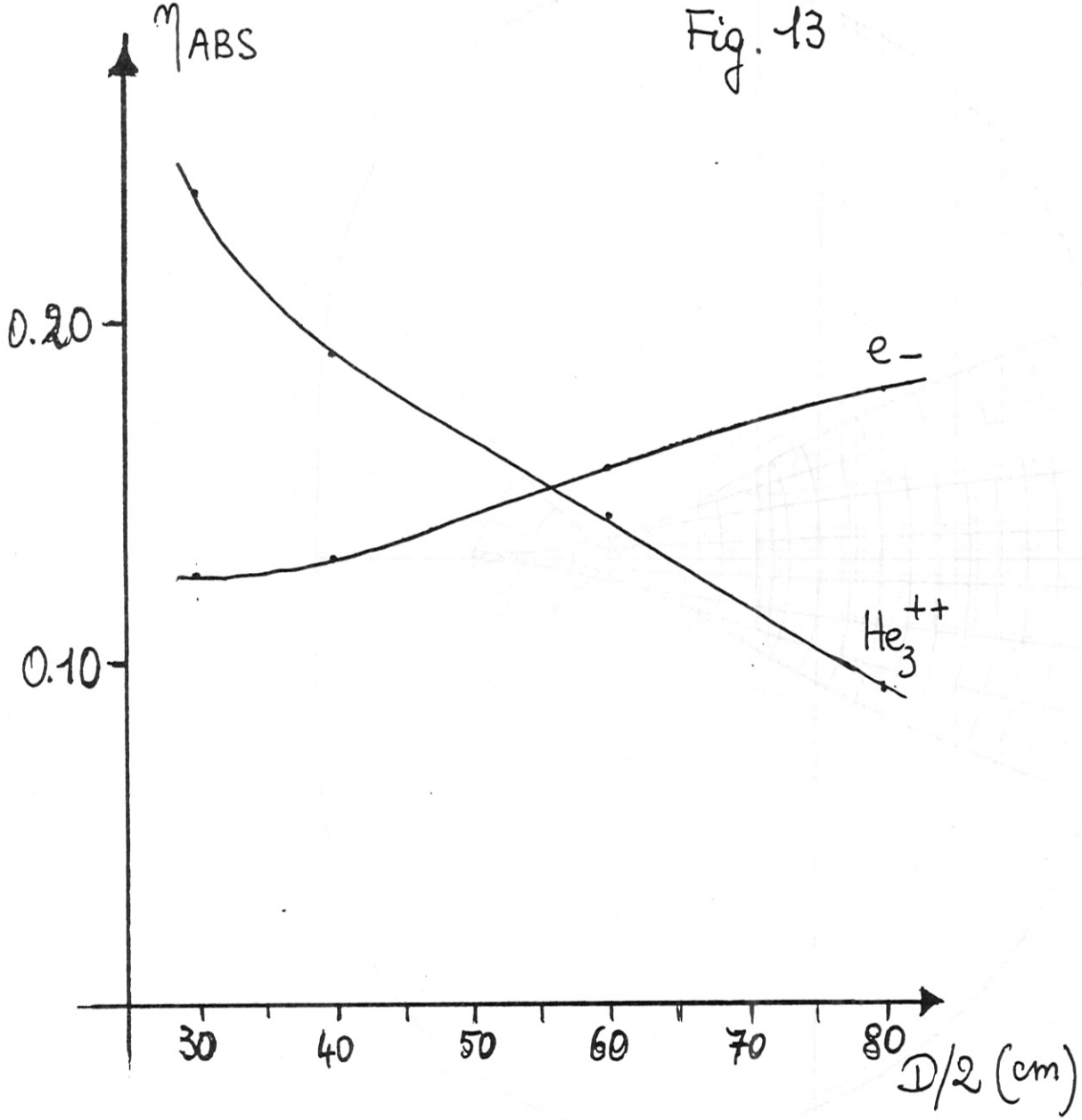

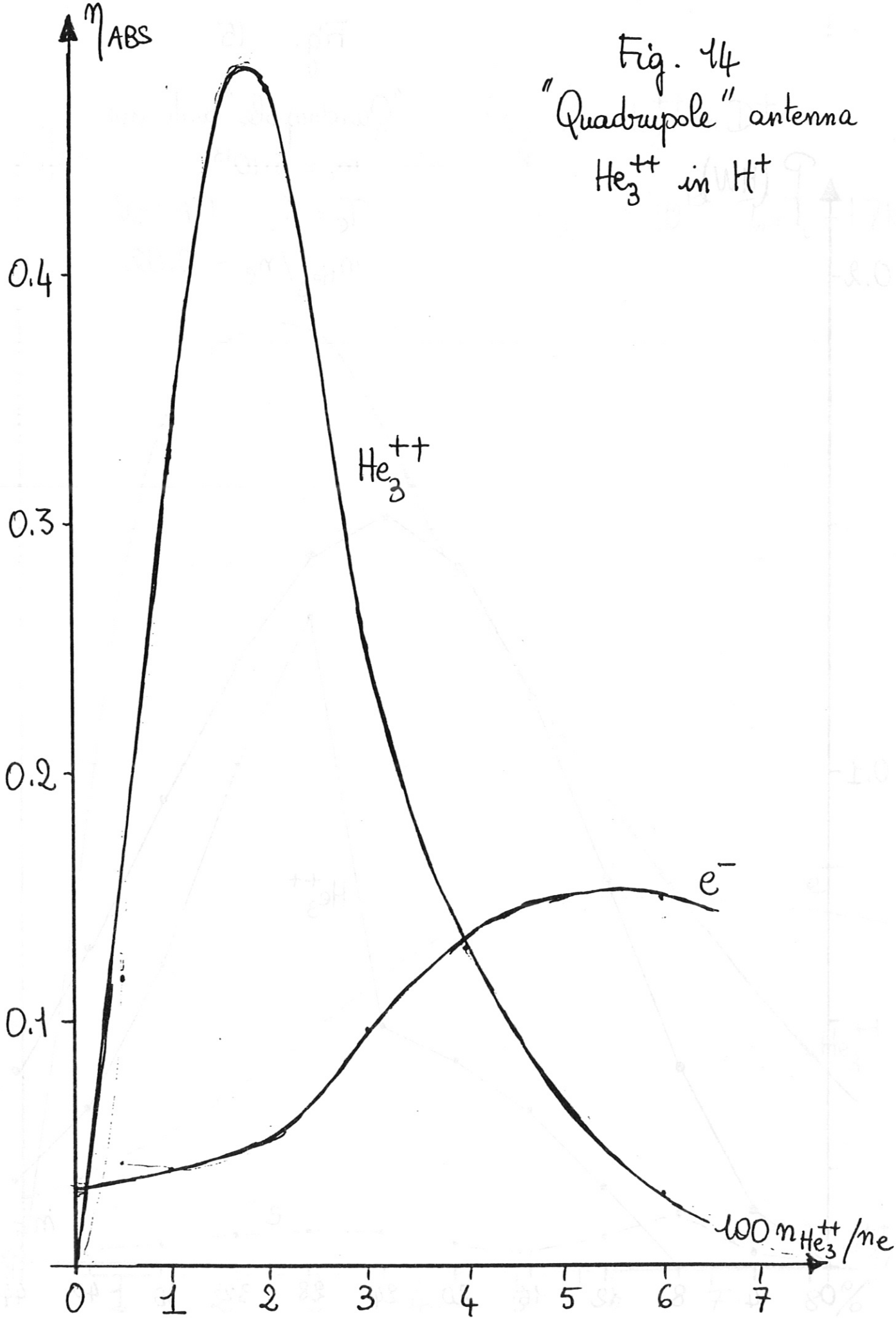

Fig. 14
"Quadrupole" antenna
He_3^{++} in H^+

Fig. 15

"Quadrupole" antenna

$n_e = 5 \cdot 10^{13}$

$T_e = T_i = 1.7$ keV

$n_{He_3}/n_e = 0.02$

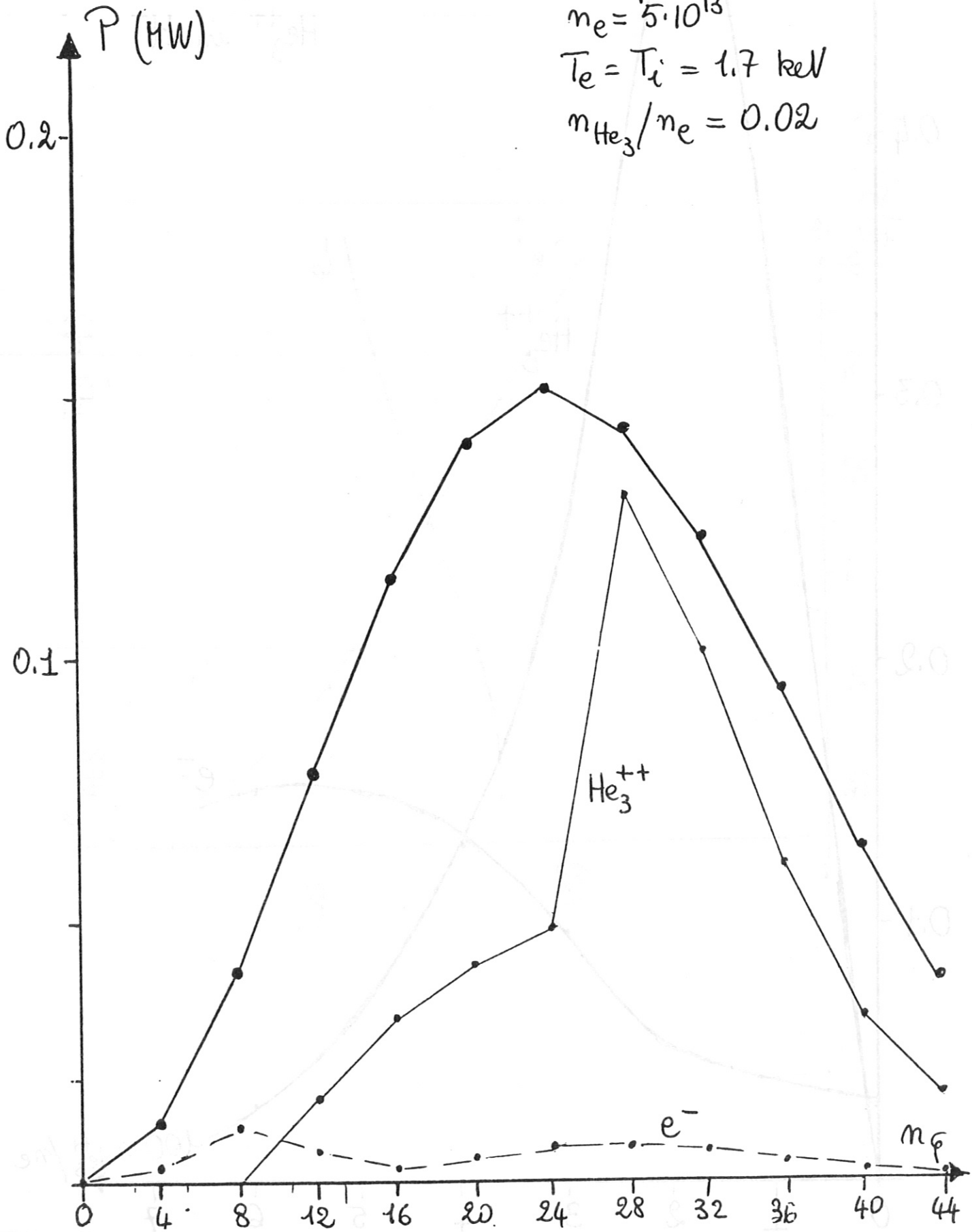

Fig. 16 - He_3^{++} in D^+

$n_e = 5 \cdot 10^{13}$ $T_e = T_i = 1.7 keV$

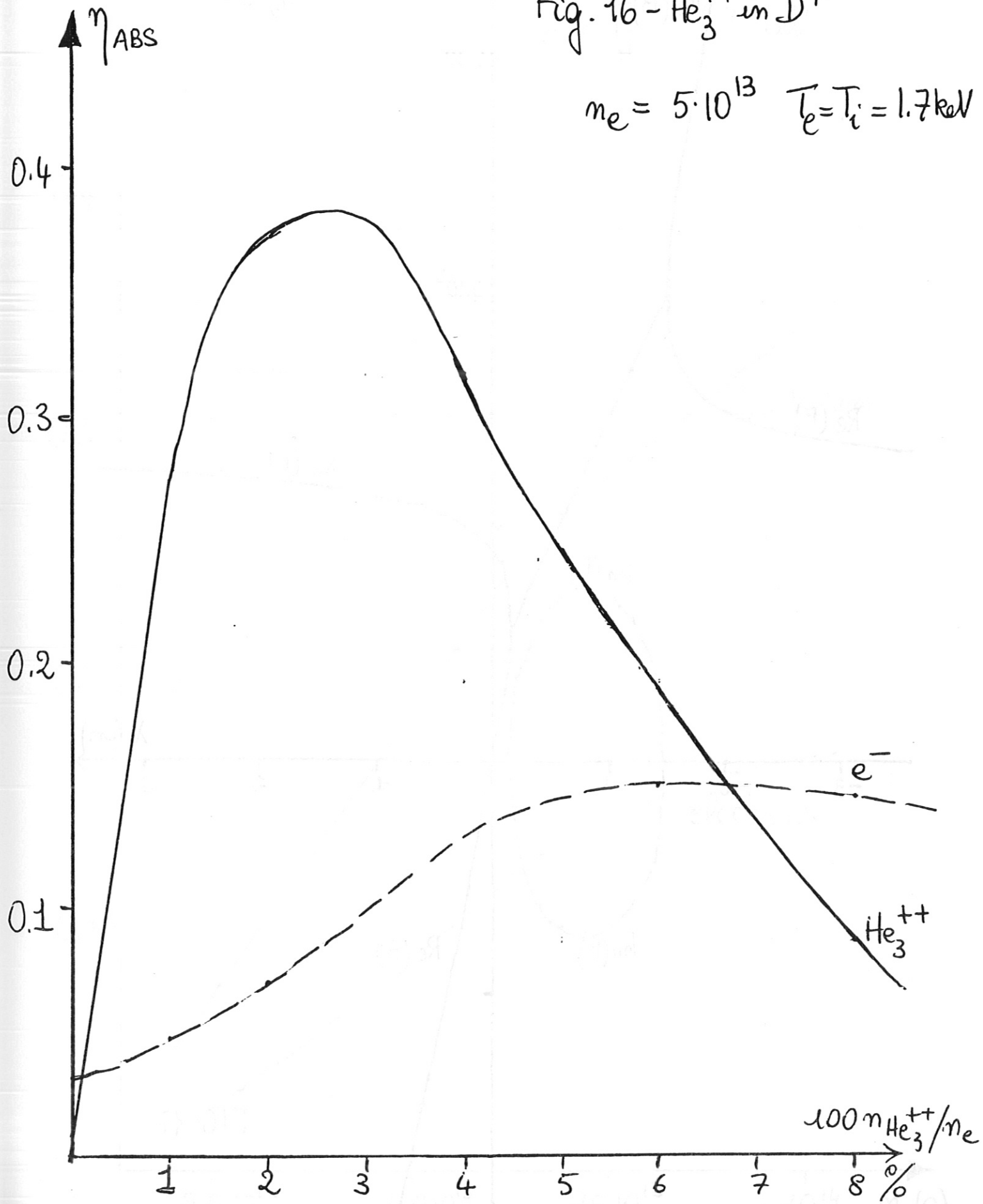

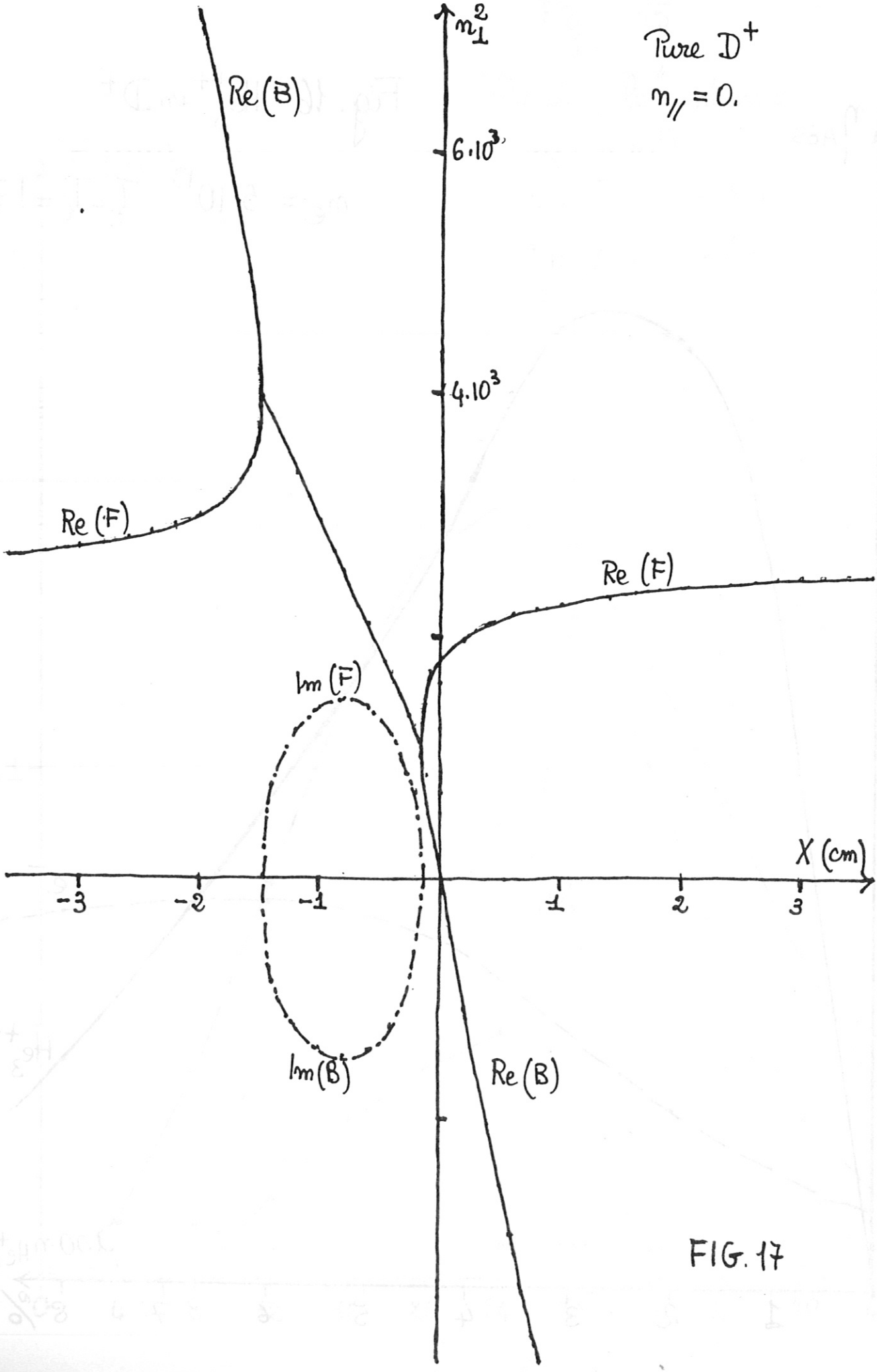

FIG. 17

Fig. 18 - 1st harm. heating of Deuterium

$\overline{T_e} = \overline{T_D} = 1.7$ keV

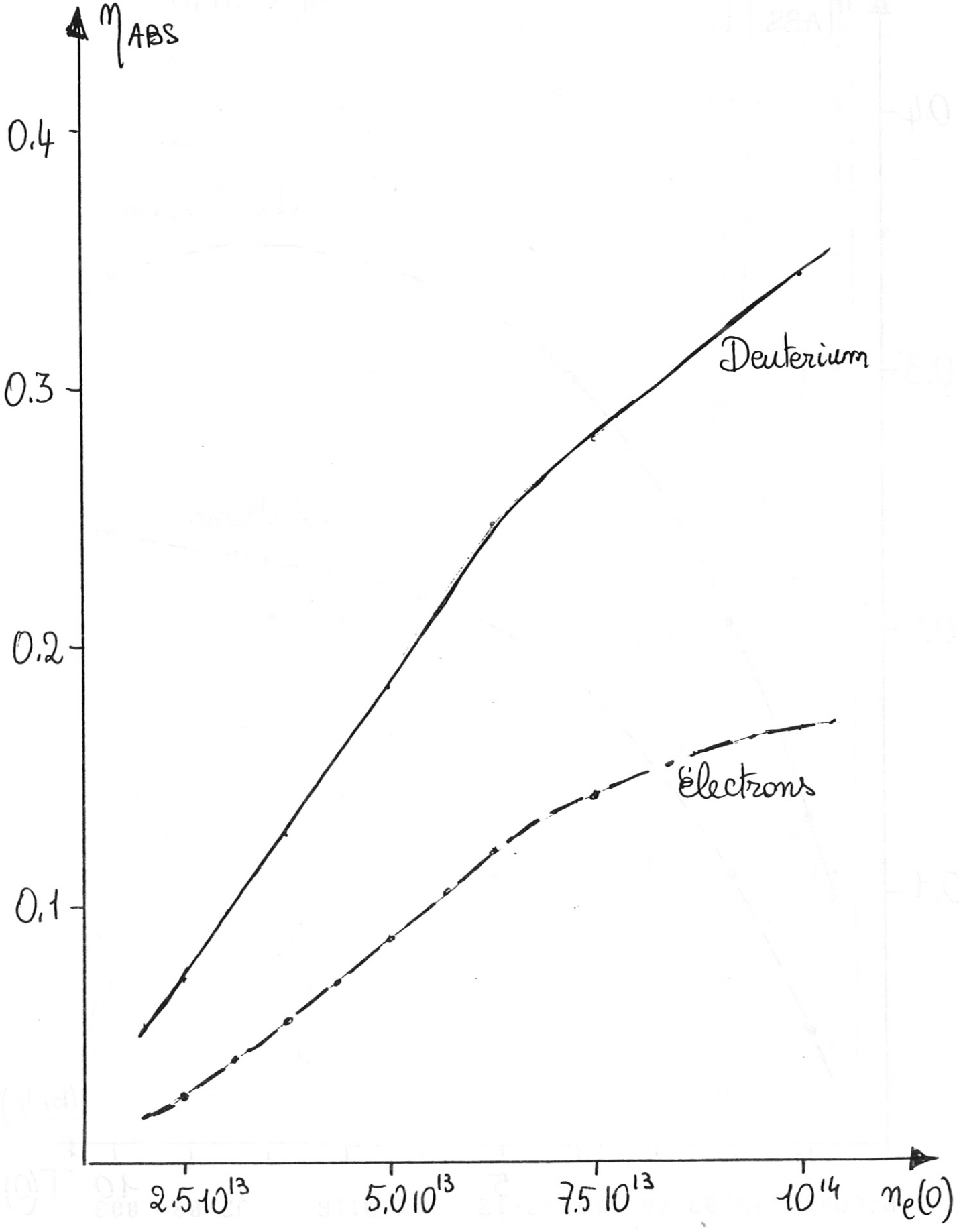

Fig. 19 - 4st harm. heating of Deuterium

$n_0 = 5.10^{13}$

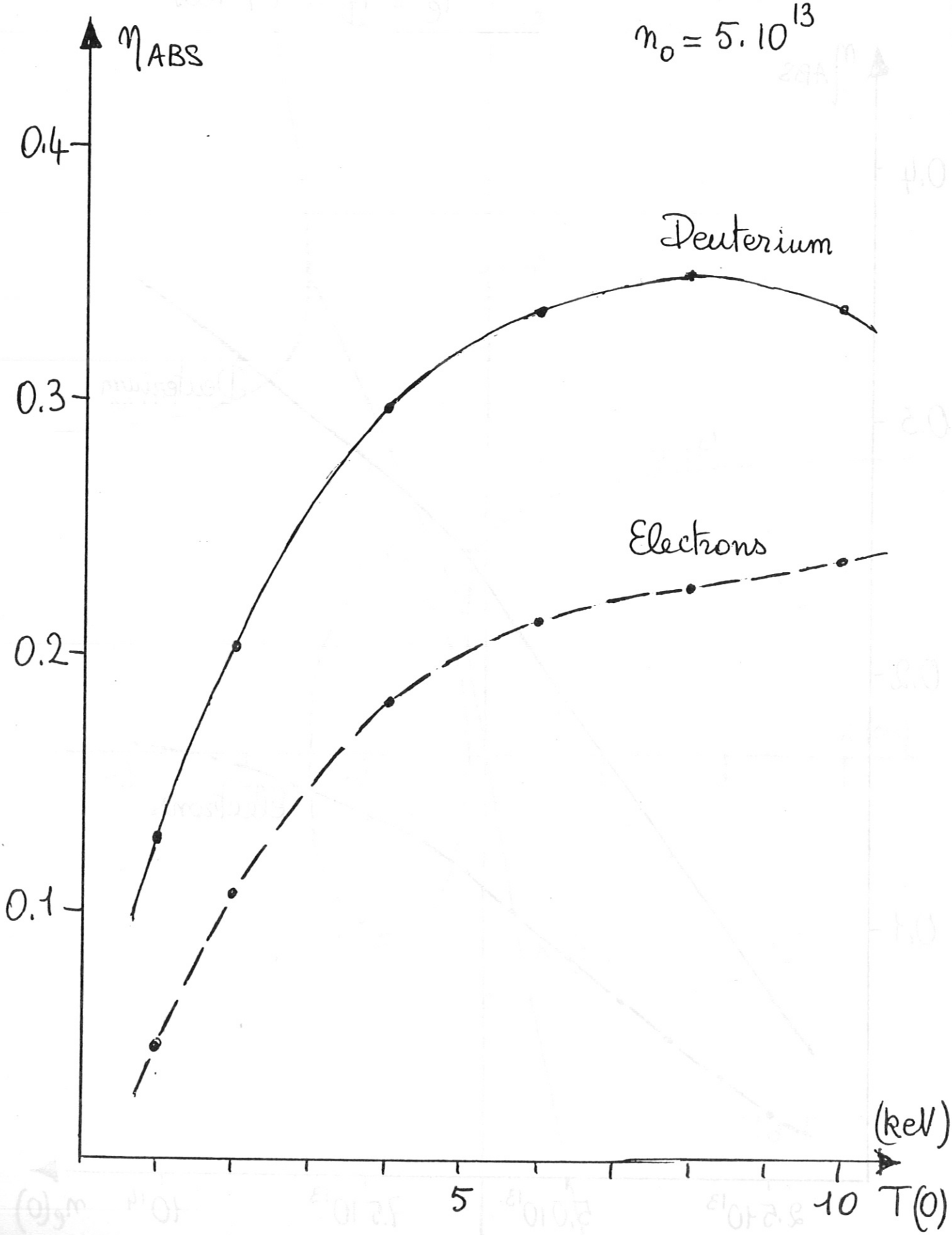

IPP-CRAY 29.03.84 14:12:12 MAB116 J2-03 003

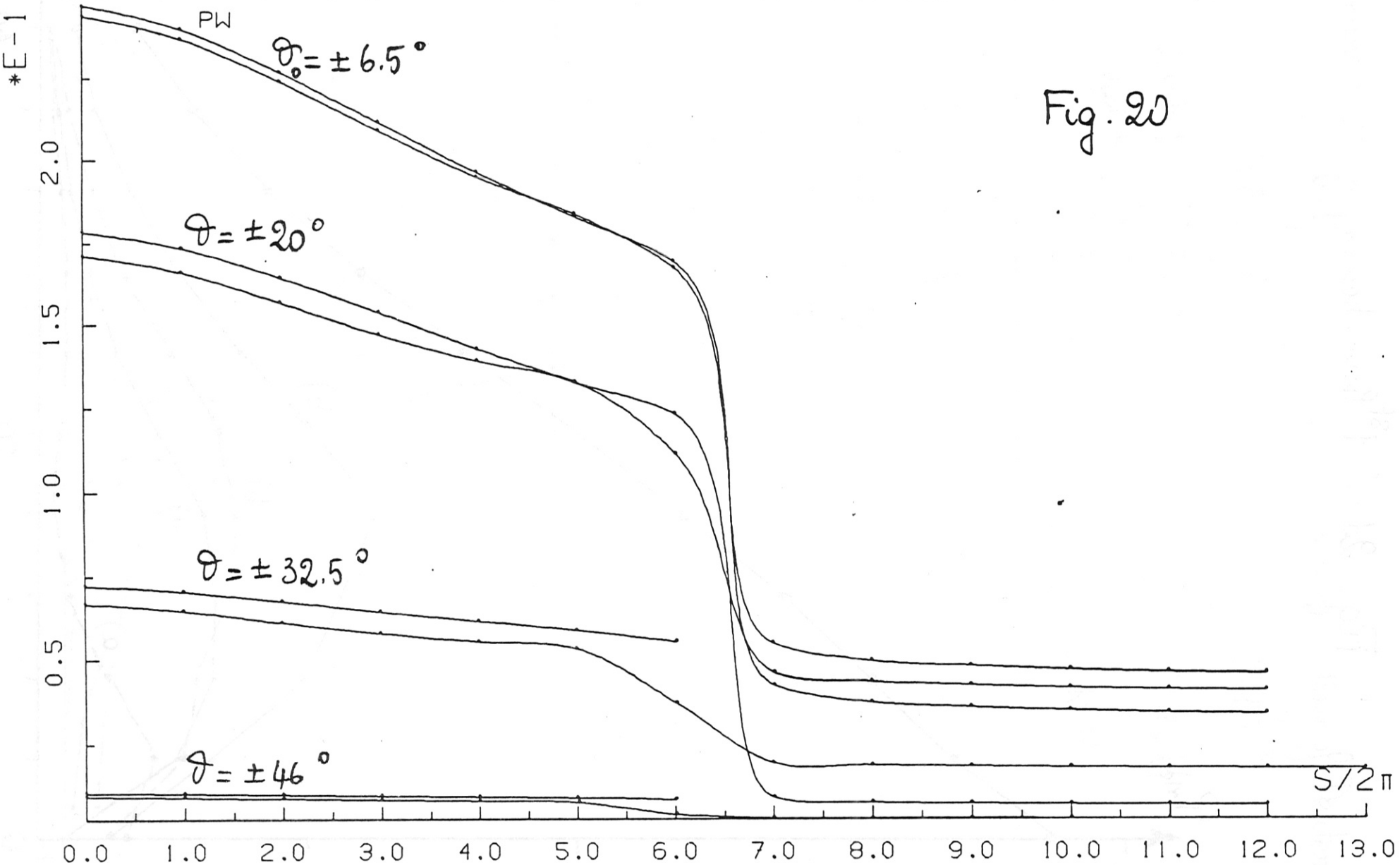

Fig. 20

Fig. 21 1st harm. heating of Deuterium

$n_e = 5 \cdot 10^{13}$

a) $T_0 = 1.7$ keV

b) $T_0 = 8$ keV

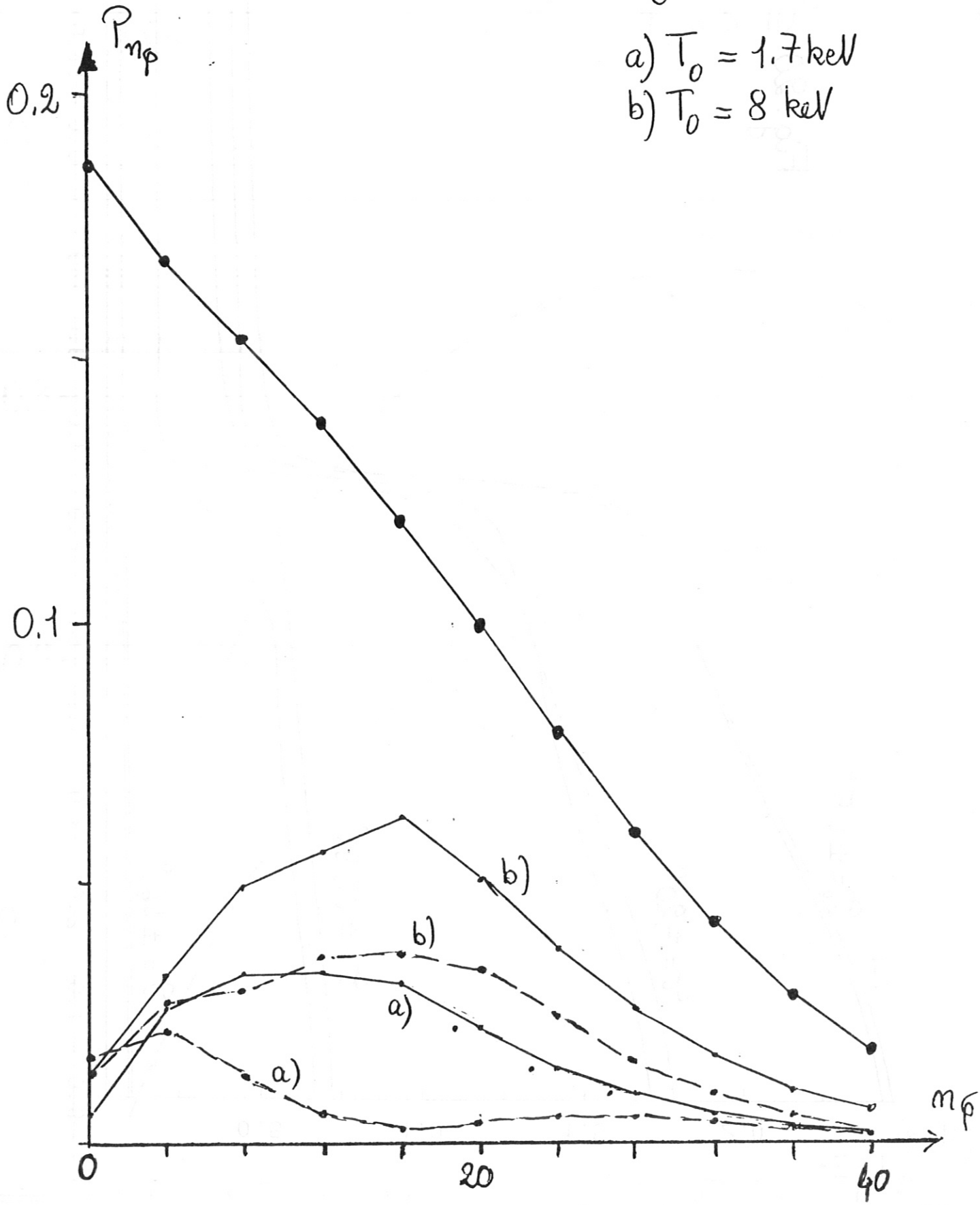

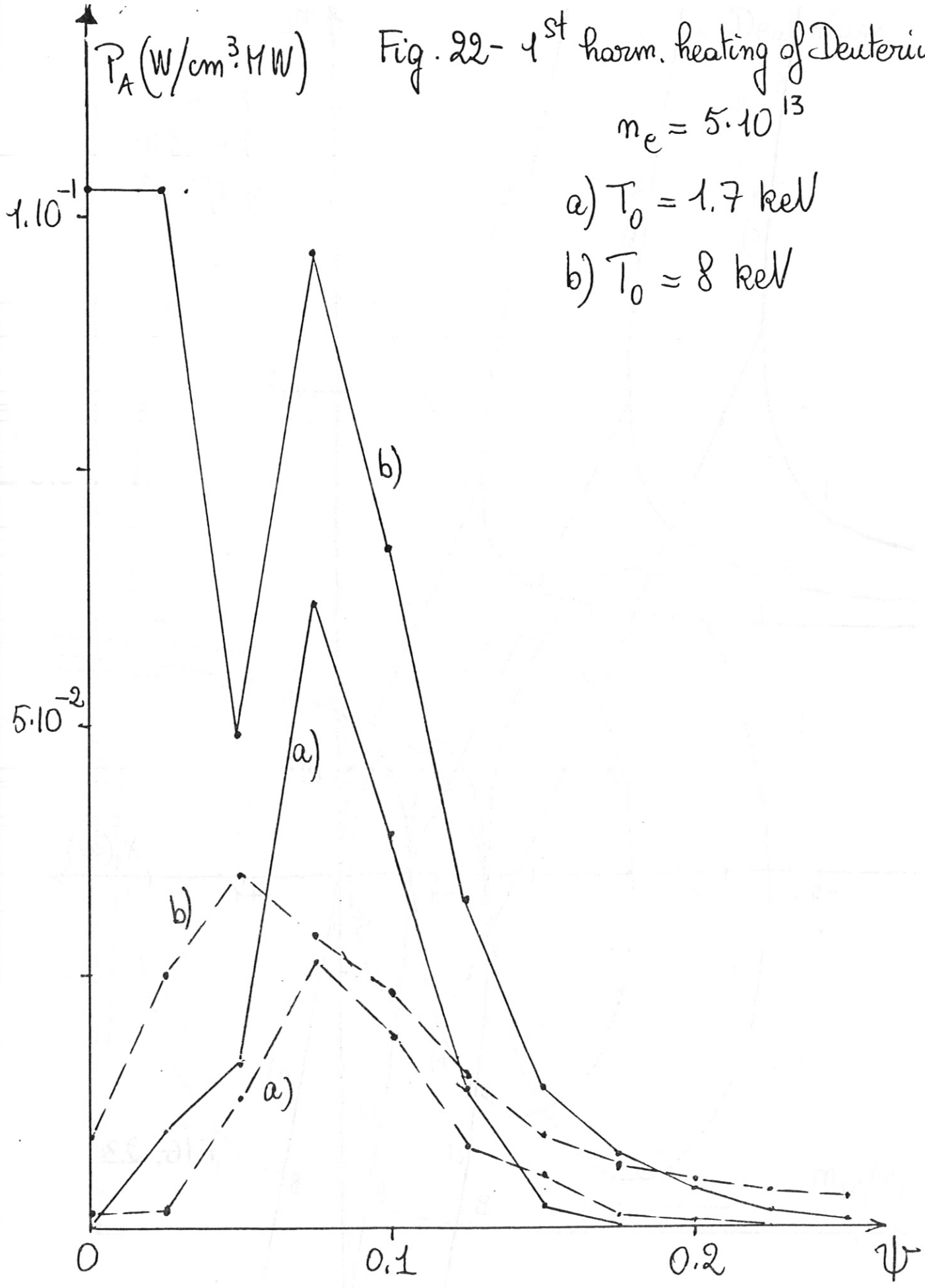
P_A (W/cm³·MW)
Fig. 22 - 1st harm. heating of Deuterium
$n_e = 5 \cdot 10^{13}$
a) $T_0 = 1.7$ keV
b) $T_0 = 8$ keV
$1 \cdot 10^{-1}$
$5 \cdot 10^{-2}$
b)
a)
b)
a)
0
0.1
0.2
ψ

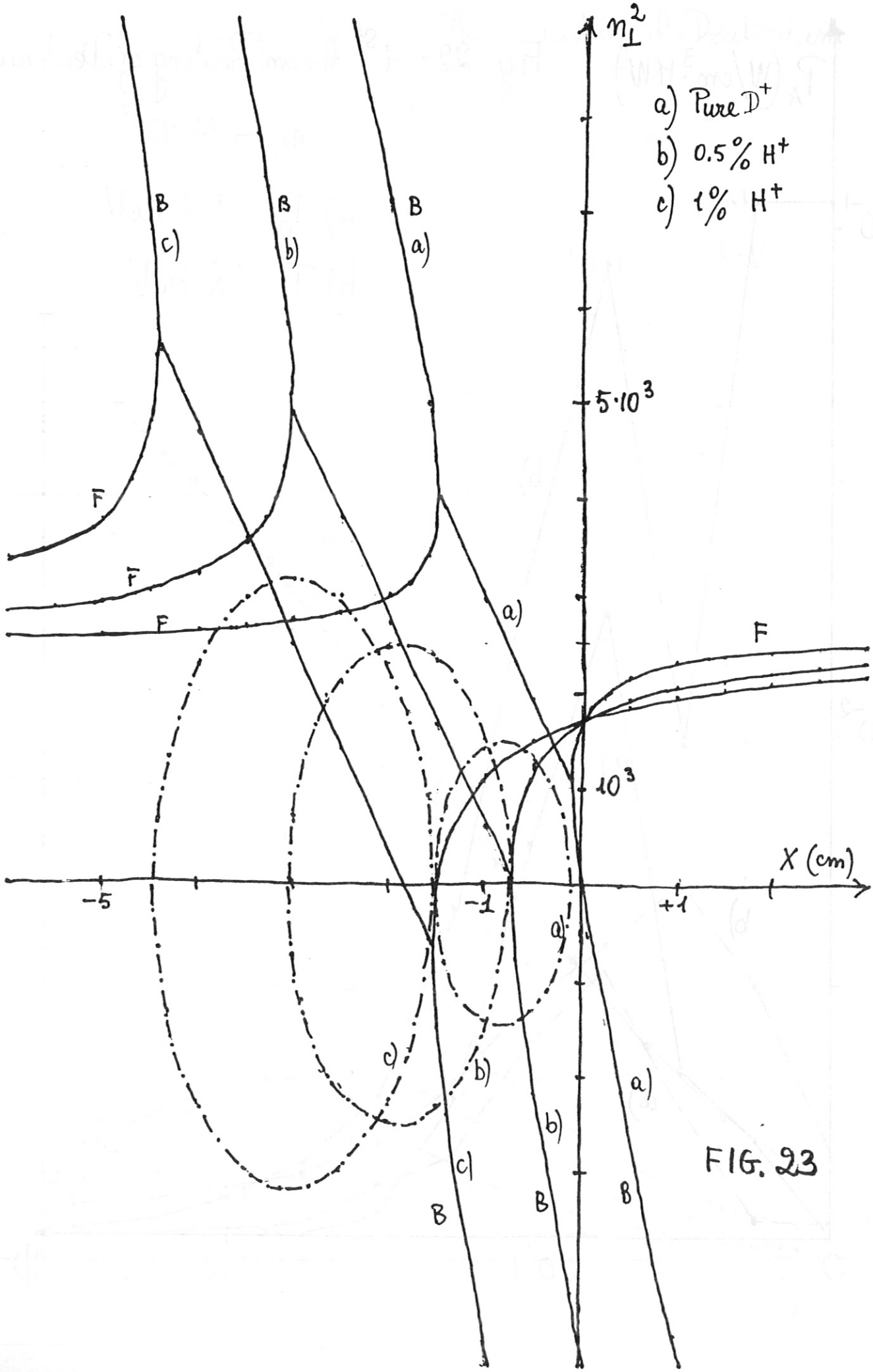
$n_\perp^2$
a) Pure D^+
b) 0.5% H^+
c) 1% H^+
B
c)
B
b)
B
a)
F
F
F
a)
F
$5 \cdot 10^3$
10^3
X (cm)
-5
-1
+1
a)
c)
b)
a)
b)
c)
B
B
B

FIG. 23

Fig. 24 H^+ in Deuterium

$n_e(0) = 5 \cdot 10^{13}$

$T_e = T_D = T_H = 1.7$ keV

$f = 50$ MHz

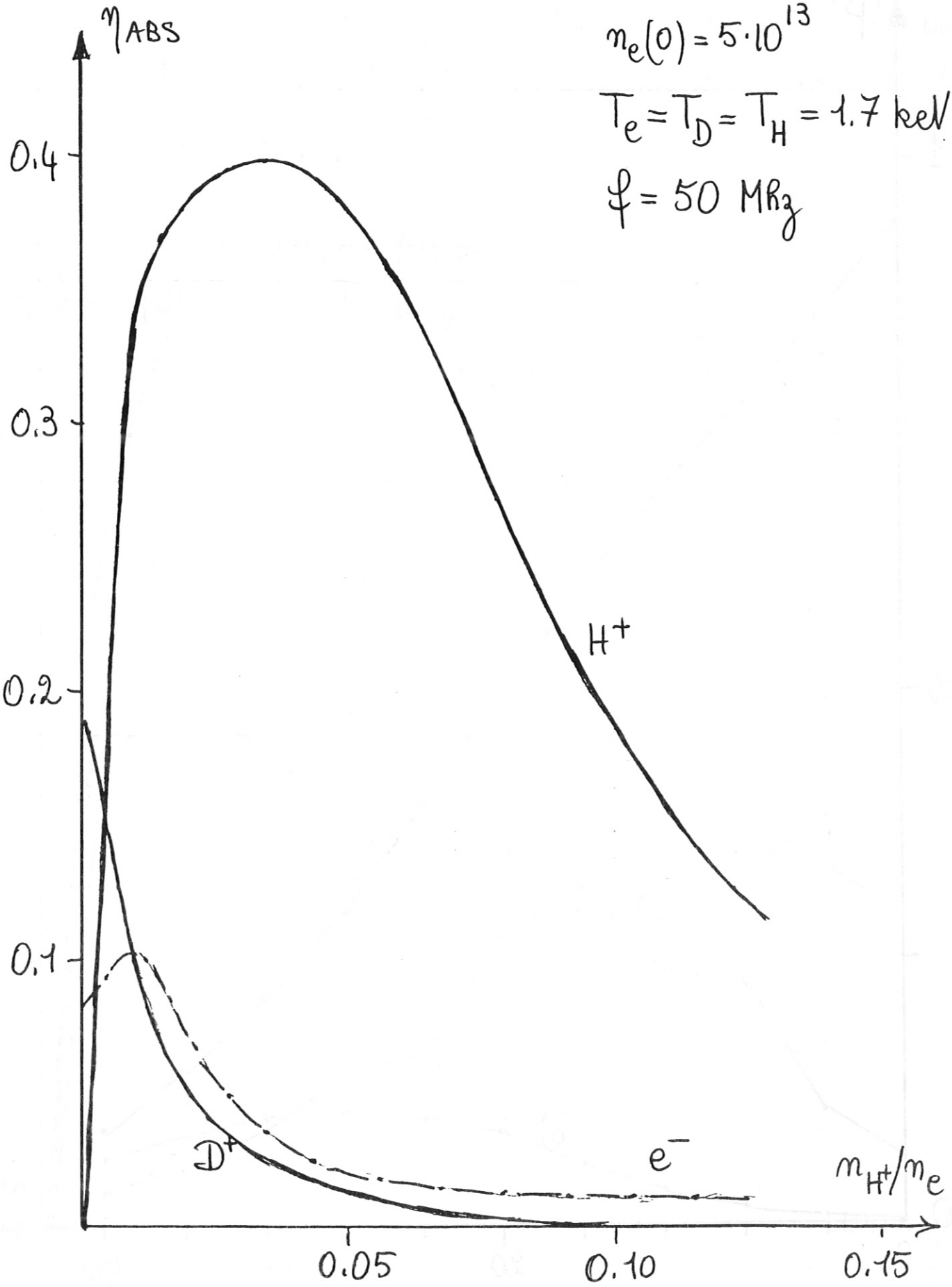

Fig. 25 - H^+ in Deuterium

a) $n_H/n_e = 0.02$

b) $n_H/n_e = 0,10$

$n_e(0) = 5.10^{13}$

$T_e(0) = T_H(0) = T_D(0) = 1.7$ keV

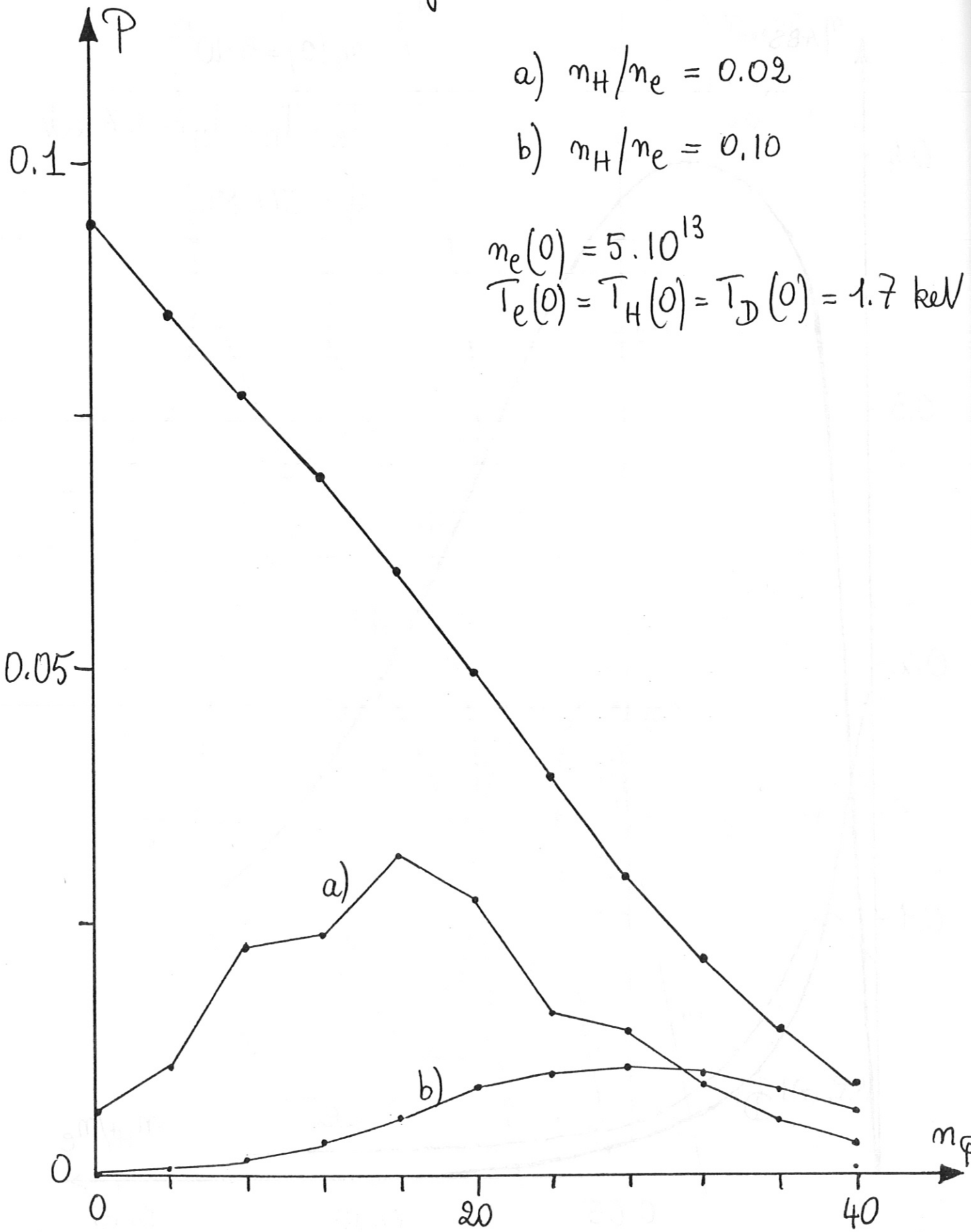

Fig. 26

a) Dipole antenna, $T_H = 1.7$ keV

b) Dipole antenna, $T_H = 5.1$ keV

c) Quadrupole antenna, $T_H = 5.1$ keV

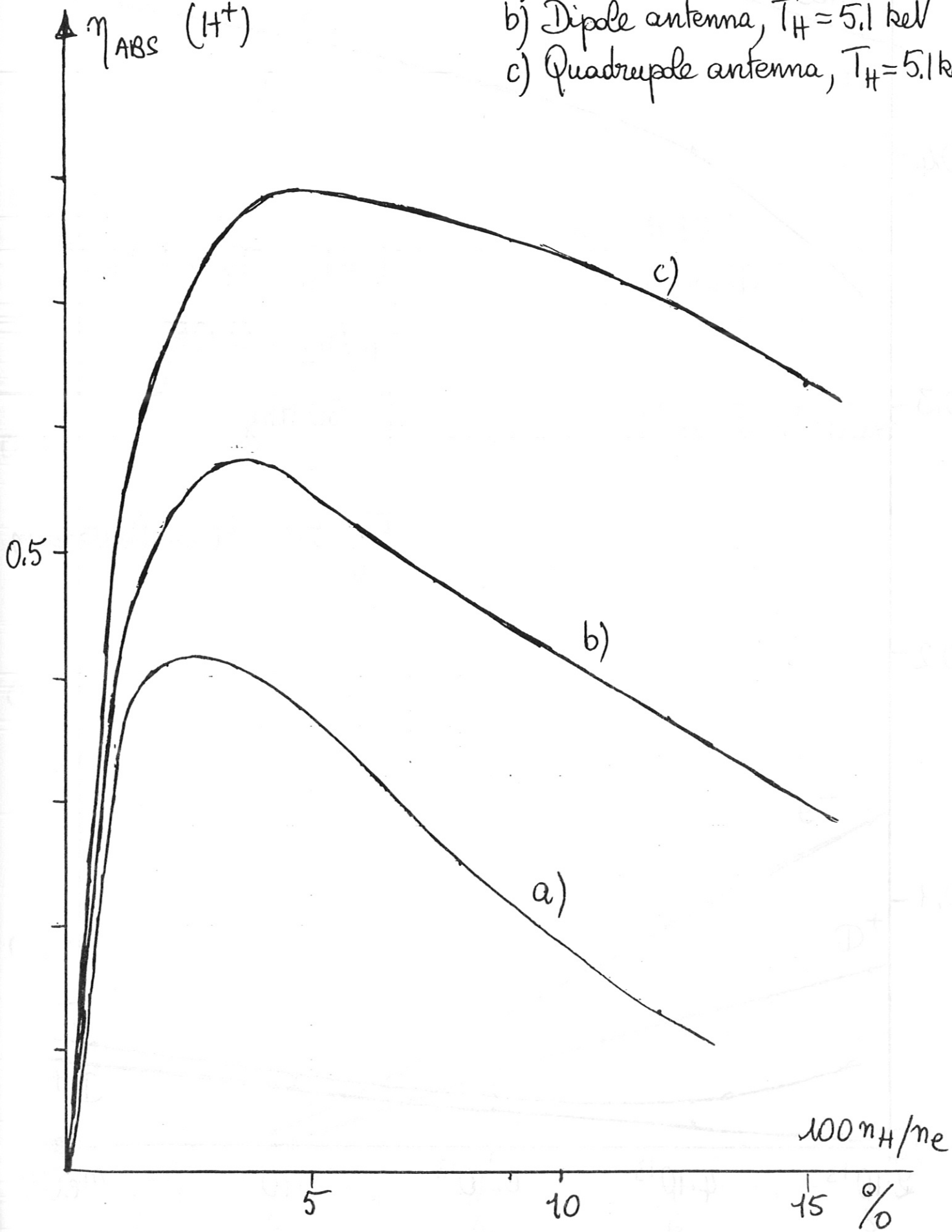

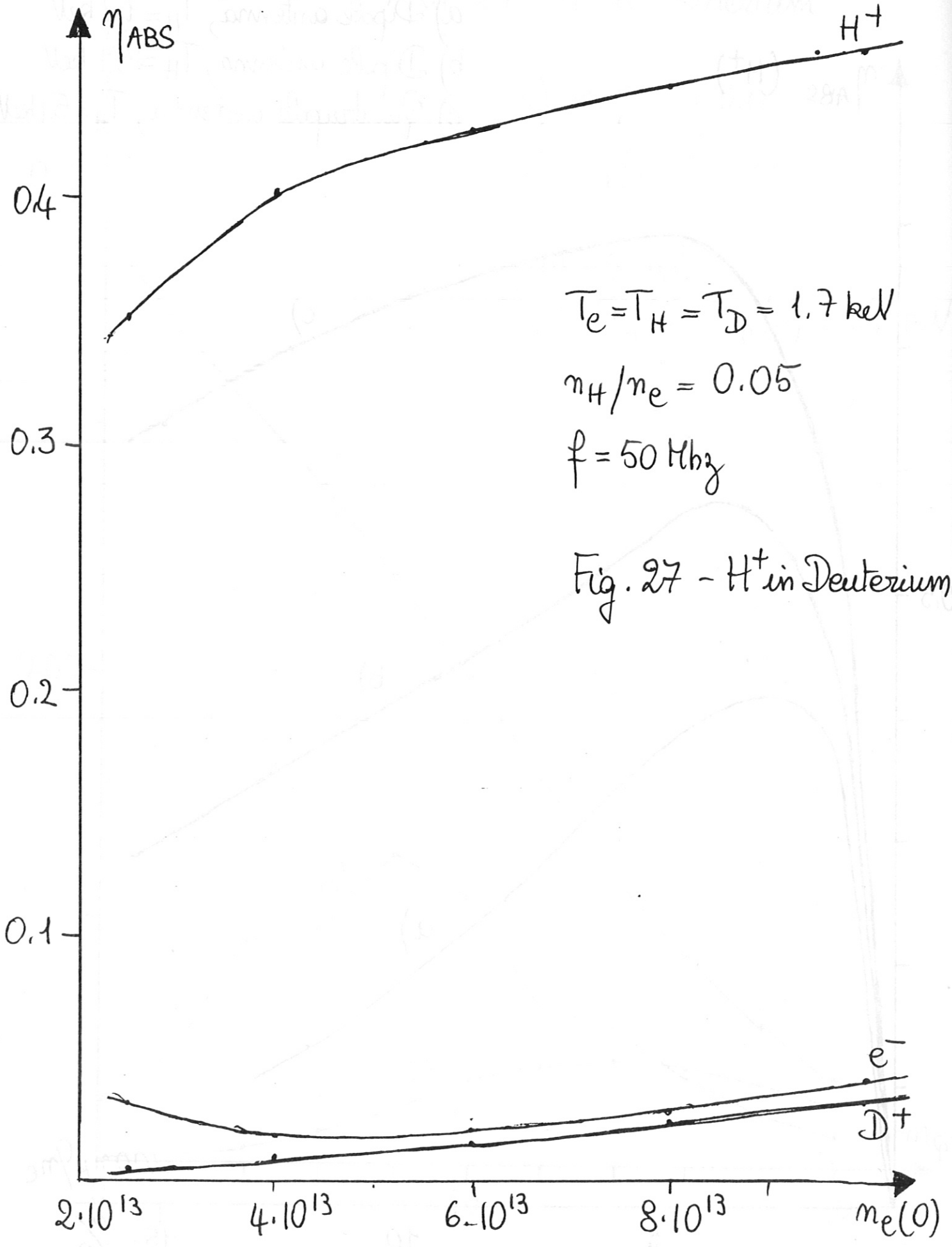

Fig. 27 - H^+ in Deuterium

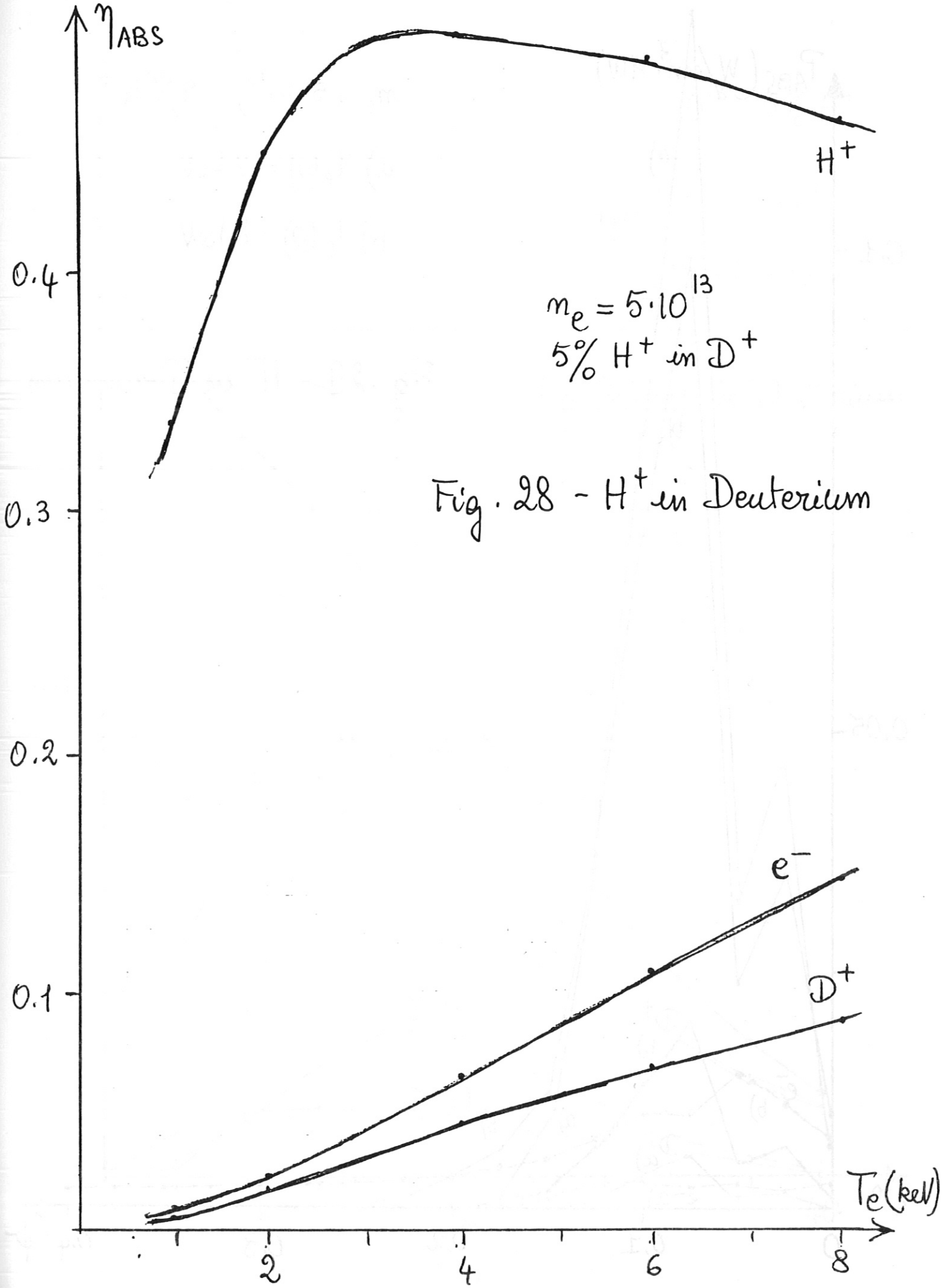

Fig. 28 - H^+ in Deuterium

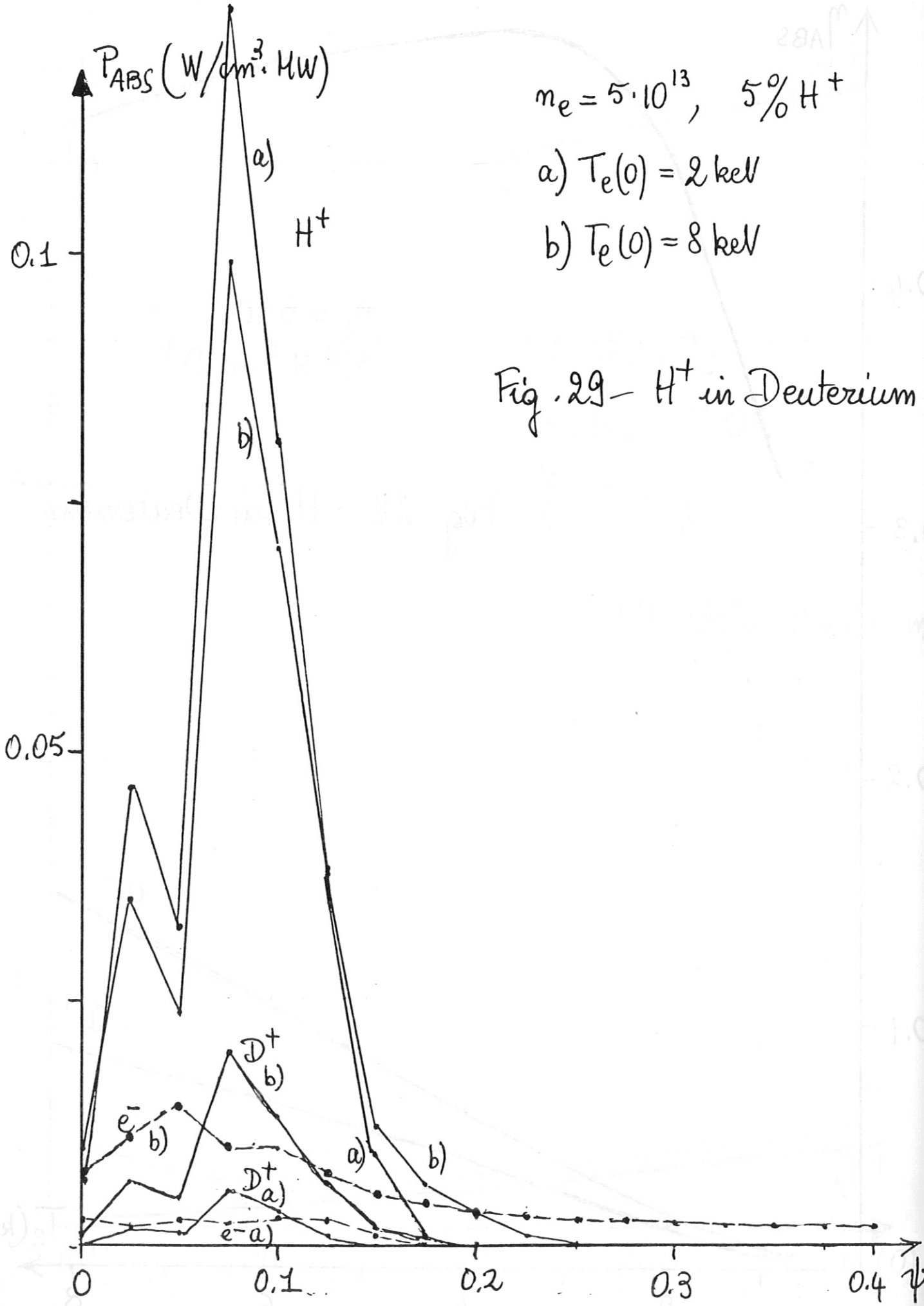

$n_e = 5 \cdot 10^{13}$, 5% H^+

a) $T_e(0) = 2$ keV

b) $T_e(0) = 8$ keV

Fig. 29 – H^+ in Deuterium

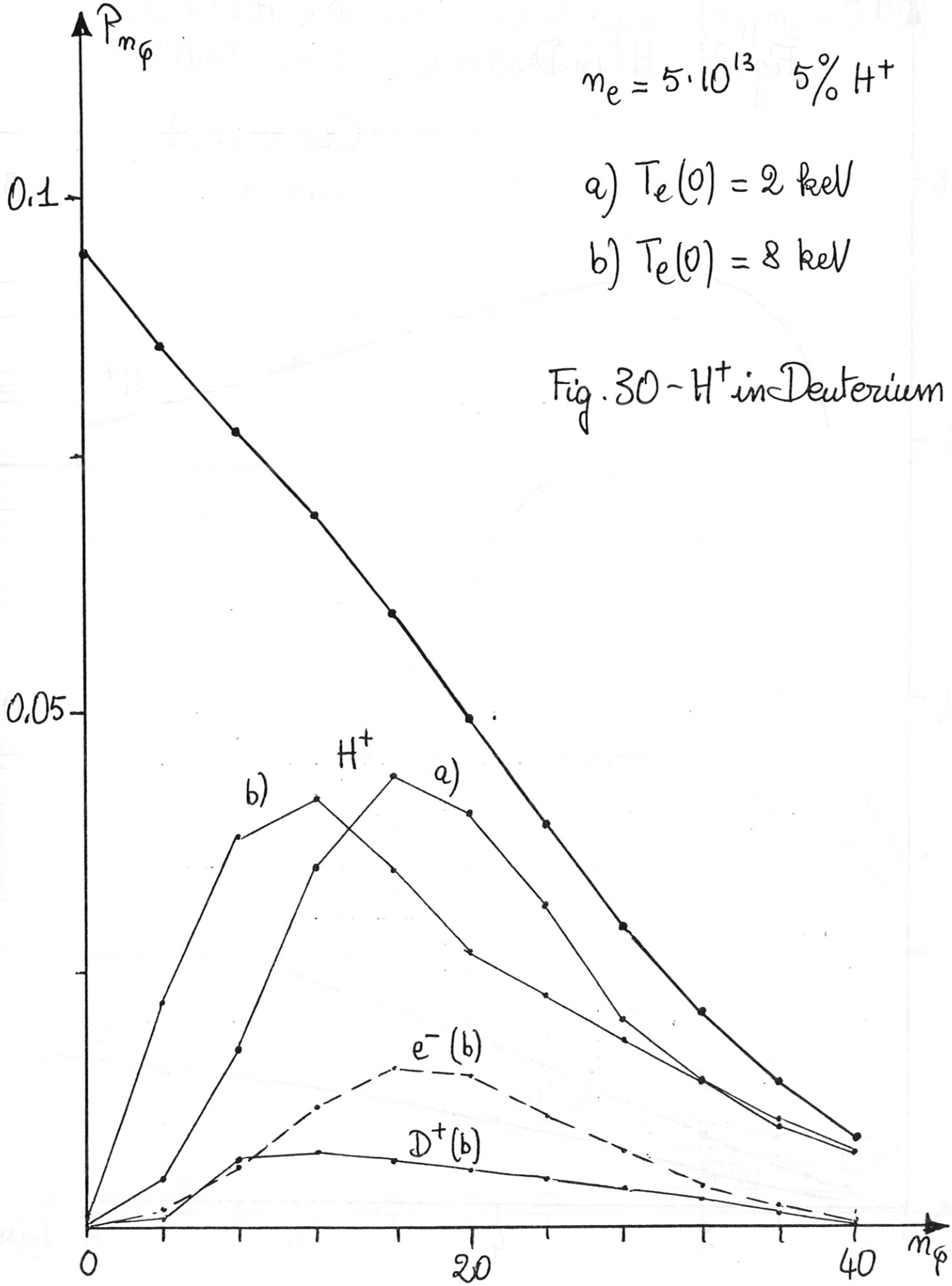

Fig. 30 - H^+ in Deuterium

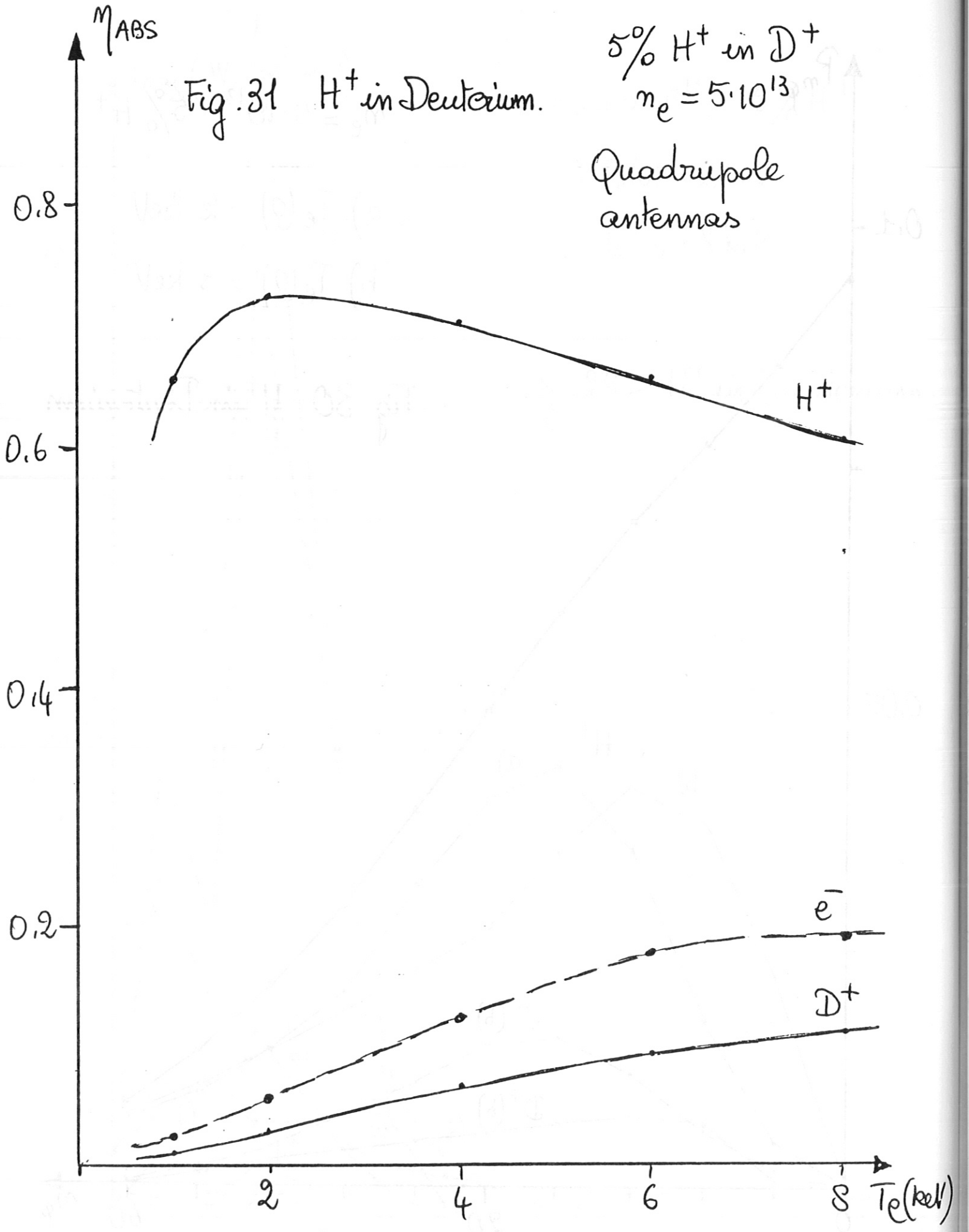
η_{ABS}
Fig. 31 H^+ in Deuterium.
5% H^+ in D^+
$n_e = 5 \cdot 10^{13}$
Quadrupole antennas
0.8
0.6
0.4
0.2
H^+
e^-
D^+
2
4
6
8
T_e(keV)

Fig. 32 - H^+ in Deuterium $(n_H/n_e = 0.05)$
Quadrupole antennas

a) $T_e(0) = 2$ keV

b) $T_e(0) = 8$ keV